DECLASSIFIE [redacted]

[redacted]

NASA TECHNICAL MEMORANDUM

NASA TM X-1197

[redacted]

NASA TM X-1197

CLASSIFICATION CHANGED
UNCLASSIFIED
TO ____________________
By Authority of [illegible]

[redacted]

~~Declassified~~ by authority of NASA
Classification Change Notices No. [illegible]
Dated ** [illegible]

AN INVESTIGATION OF THE APOLLO AFTERBODY PRESSURE AND HEAT TRANSFER AT HIGH ENTHALPY

by George L. Fox and Joseph G. Marvin

Ames Research Center
Moffett Field, Calif.

U. S. Government Agencies and Contractors Only

NATIONAL AERONAUTICS AND SPACE ADMINISTRATION • WASHINGTON, D. C. • MARCH 1966

[redacted] NASA TM X-1197

AN INVESTIGATION OF THE APOLLO AFTERBODY PRESSURE AND HEAT TRANSFER AT HIGH ENTHALPY

By George L. Fox and Joseph G. Marvin

Ames Research Center
Moffett Field, Calif.

[redacted]

[redacted]

[redacted]

NATIONAL AERONAUTICS AND SPACE ADMINISTRATION

[redacted]

U. S. Government Agencies and
Contractors Only

[redacted] DECLASSIFIED

AN INVESTIGATION OF THE APOLLO AFTERBODY PRESSURE AND HEAT TRANSFER AT HIGH ENTHALPY*

By George L. Fox and Joseph G. Marvin
Ames Research Center

SUMMARY

15852

Pressure, heat-transfer, and flow-visualization data for a model of the Apollo at a total stream enthalpy of 4500 Btu/lb, $M_\infty = 10$, and $Re_{\infty_D} = 120,000$ showed that the flow separated from the afterbody at an angle of attack (α) of 0°, attached on the windward meridian near $\alpha = 23^\circ$, and was attached over most of the windward surface for $\alpha \geq 33^\circ$.

At $\alpha = 33^\circ$, the pressure and heating-rate distributions on the most windward meridian of the afterbody were predicted adequately by two-dimensional blunt-plate theory, but at $\alpha = 44^\circ$ and 23°, this theory was not adequate. At $\alpha = 0^\circ$, the afterbody pressures were predicted by a method which did not depend on a priori knowledge of the flow-separation direction.

Analysis of the flow chemistry along a streamtube close to the body surface showed that the inviscid flow over the afterbody was probably frozen for the test conditions of the present investigation. Extending this analysis to the full-scale Apollo at peak heating showed either frozen or equilibrium afterbody flow can be expected depending on the trajectory considered.

Autha

INTRODUCTION

Experimental pressure and heat-transfer data on models of the Apollo configuration have been published by many investigators. No attempt will be made to reference all of these, but references 1 and 2 presented some data obtained in the Ames 1-foot shock tunnel. In these references, no detailed discussion regarding the test models, procedures, and test conditions was given and only selected portions of all the data were used.

It is the purpose of this report to present all the pressure and heat-transfer data taken in the Ames 1-foot shock tunnel on sting-supported models of the Apollo. In addition, the flow chemistry over the models was analyzed and the results are presented. The data and the flow chemistry analysis are interpreted as they apply to a full-scale vehicle at several flight conditions.

[redacted]

[redacted]

SYMBOLS

C	specific heat
h	local enthalpy
l	model skin thickness
M	Mach number
N	nitrogen atoms
O	oxygen atoms
p	pressure
Pr	Prandtl number
$\dot{q}$	heat-transfer rate
R	model radius (see fig. 2(a))
Re	Reynolds number
R_n	nose radius (see fig. 2(a))
r	radius from axisymmetric axis to body surface or dividing streamline
S	surface distance from axis of symmetry
S^*	defined by equation (A1)
T	temperature
t	time
U^*	dimensionless dividing streamline velocity, u_d/u_e
u	velocity
x	surface distance from stagnation point
$[X_i]$	$\dfrac{\text{number of } i \text{ species atoms}}{\text{total number of } i \text{ species combined, free, and ionized}}$
$[X_i]_{qe}$	equilibrium value of species number as fraction based on nonequilibrium temperature
$[Y_i]$	$\dfrac{\text{number of } i \text{ species ion}}{\text{total number of } i \text{ species combined, free and ionized}}$

[redacted]

Z	$\frac{h_r - h_w}{h_s - h_w}$
α	angle of attack
γ	isentropic exponent
μ	viscosity
ρ	density
φ	meridian angle around model
ω	viscosity law coefficient

Subscripts

a	average afterbody conditions
D	diameter
d	conditions along dividing streamline
e	boundary-layer edge conditions
N	nitrogen atoms
O	oxygen atoms
r	recovery conditions
s	stagnation-point conditions
t	total conditions
w	wall conditions
1	ahead of shock wave
2	behind normal shock wave
∞	free-stream test conditions

Superscript

$'$	reference enthalpy conditions

[redacted]

TEST APPARATUS

Test Facility

The tests were performed in the Ames 1-foot shock tunnel shown schematically in figure 1. The test gas is compressed to a high enthalpy ($h_t = 4500$ Btu/lb) and pressure ($p_t = 4000$ psia) by a combustion-driven shock wave reflected off the end of the driven tube. The gas is then expanded through a conical nozzle into a 1-foot-square test section. The conical nozzle has a 9° total angle, a 0.22-inch-diameter throat, and a 1-foot-diameter exit. The test stream has the following nominal test-section conditions: $M_\infty = 10$, $Re_\infty/\text{foot} = 60{,}000$, $p_\infty = 0.017$ psia, and $p_{t_2} = 2.8$ psia.

Both analysis of the test-stream calibration data and nonequilibrium calculations showed that about 3-percent atomic oxygen was frozen in the free stream. No corrections were applied to the data to take account of this small free-stream dissociation.

Further details regarding the operation of the tunnel may be found in reference 3.

Models and Instrumentation

The models used in these tests are shown in figures 2 and 3. The basic shape represents the Apollo command module.

Pressure model.- The pressure model was machined from brass and had walls 1/16 inch thick. The front face was removable for access to the pressure cells. Five pressure cells were located in the afterbody as indicated in figure 2(a). Figure 2(b) is a photograph of the cell installation.

Capacitance-type pressure cells were used in these tests (see fig. 2(c)). Basically, these cells operate when pressure acts against the face of a diaphragm deflecting it toward a backing plate causing a change in capacitance between the diaphragm and the backing plate. Each cell was electrically connected as one leg of a capacitance bridge circuit driven by a 100 kilocycle power source. The capacitance change of the cell caused an unbalance of current in the bridge circuit which was converted to a direct-current signal readout on a recording oscillograph.

Heat-transfer model.- The heat-transfer model is shown in figure 3. The afterbody was formed of 0.010-inch-thick type 302 stainless steel sheet. A.W.G. No. 36 chromel-constantan thermocouple wire was butt welded to the inner surface in four rows. The front face was made of brass and was nominally 0.125 inch thick.

Model support arrangement.- The models were positioned at different angles of attack by a bent sting adapter which connected the model sting to a stationary strut in the test section. The angles of attacked were 44°, 33°,

[redacted]

23°, 16°, and 2.5°. The sting was brought out of the apex of the conical afterbody at an angle of 30° to reduce the flow disturbance along the windward ray. (See fig. 2(a).) A wedge cover was attached to the sting to minimize interference and provide a conduit for the instrumentation leads.

TEST METHOD AND DATA REDUCTION

Pressure Measurements

The pressure cells were calibrated before and after each pressure test. Known pressures were applied to the gages and the resulting oscillograph deflection was recorded. These calibrations were normally repeatable within ±2 percent. The model pressures and test-section pitot pressure were recorded continuously during the test runs.

The data are presented as the ratio of model pressure to pitot pressure, p/p_{t_2}. The accuracy of this ratio is limited primarily by the response of the pitot probe to pressure fluctuations and to vibrations of the test section caused by shock interactions in the shock tube. The maximum ratio error is estimated to be ±10 percent of the measured value.

Heat-Transfer Measurements

The heat-transfer rate was measured by the thin-skin transient-temperature technique which is based on the following calorimetric equation

$$\dot{q} = \rho C l \frac{dT}{dt}$$

Flow was established over the isothermal model within 1 or 2 msec and the rise in skin temperature with time was recorded on an oscillograph. The temperature-time traces were curve-fitted by a digital computer and the resulting heating rates computed at 5 msec intervals from time-zero to 20 msec. Time-zero was specified as the time at which the wall temperature started to increase. The maximum temperature rise at any measured point on the model during this time interval was less than 16° F. Therefore the effect of the nonisothermal wall on the boundary layer and as a potential for skin conduction is considered negligible.

The data are presented as $\dot{q}/\dot{q}_{s_{\alpha=0}}$. The value of heat transfer $\dot{q}_{s_{\alpha=0}}$ was obtained from the measured heat transfer at the stagnation point of a hemisphere which was run along with the test model. The hemisphere was mounted outside the bow shock region of the model and did not interfere with the afterbody measurements. The value of $\dot{q}_{s_{\alpha=0}}$ is given by

$$\dot{q}_{s_{\alpha=0}} = 0.456\dot{q}_{s_{\text{hemisphere}}}$$

where the factor 0.456 accounts for the difference in velocity gradients between the Apollo model and the hemisphere due to the differences in radii and shape. The effect of shape is to increase the velocity gradient by about 14 percent (see, e.g., ref. 4).

Flow Visualization

To aid in interpreting the afterbody pressure and heat-transfer measurements, the flow patterns over the model were made visible. Two techniques were used. First, graphite grease was mixed with vacuum pump oil to a consistency that would stand in small droplets and yet flow easily under the influence of shear caused by the air flow. These droplets were placed over the model before the start of the test. In regions of attached flow, the shear of the air flow caused the oil droplets to move in a streamline direction. When the flow was separated from the body, the shear was so small that there was no oil drop movement. After the test, the flow pattern of the oil drops on the model was photographed so that the regions of attached flow could be identified.

The second technique defined the flow pattern of the wake region with no sting interference while the model was at zero angle of attack. During earlier tests graphite grease on the front face of the model vaporized and formed a luminescent trail in the wake region which could be photographed. A free-flight model was machined from solid brass and supported by nylon threads from a rod spanning the top of the test section. Two thin strips of grease were placed in a cruciform shape on the front face on the model in a position perpendicular and parallel to the camera so that top and side cameras would each photograph an edge of the defined wake region. The strips were narrow so that the vapor would not fill the whole wake region. When the air flow was started, the hot air stream burned off the nylon threads and left the model in free flight with the mixing region defined by the luminous grease vapors.

RESULTS AND DISCUSSION

Data Presentation

Pressures.- The measured afterbody pressure ratios p/p_{t_2} are plotted versus S/R for various α in figure 4. The pressure ratio on the windward ray decreases with distance along the surface for $\alpha = 23^\circ$ and greater. This behavior is similar to what occurs on blunt bodies with attached flow (e.g., consider the pressure distribution for a blunted flat plate). For $\alpha = 16^\circ$ and 2.5°, the pressure ratio is essentially constant along the afterbody. This usually indicates a region of separated flow for this configuration. The pressures on the rays $\varphi = 90^\circ$ and 180° also were fairly constant over the entire range of α, indicating that the flow near these locations was separated

In figure 5 the afterbody pressures on the $\varphi = 0^\circ$ meridian are cross-plotted as a function of α for fixed S/R. There is a rapid change in pressure for α greater than 23°. This clearly points to a change in the flow pattern over the body when the flow attaches to the afterbody surface as will be indicated later during the discussion of the flow visualization tests.

Since the flow appears to be separated during some of the tests, there is a question of sting interference which may cause the afterbody pressures to differ from those for a sting-free model. To investigate this, the afterbody pressure on the Apollo configuration was measured recently in this same facility (ref. 2). The sting-free data at $\alpha = 0^\circ$ are within a few percent of the present data, indicating small sting effects on the pressures in the separated regions. A comparison with these data is given later.

Heat transfer.- The normalized afterbody heat-transfer distributions are plotted for various angles of attack in figure 6, and the windward meridian data are cross-plotted in figure 7. No data were taken at $\alpha = 16^\circ$. The heating-rate distributions follow the same trends as the pressure distributions. Again, the data indicate that the afterbody flow is attached on the windward surface for angles of attack greater than 23°. The data for $\alpha = 2.5^\circ$, where the flow is separated (fig. 6(d)), vary considerably around the afterbody probably because of sting interference. As stated earlier, there seemed to be very small interference effects in the pressure measurements at this angle of attack; however, the sting could influence the local surface boundary-layer flow more than the pressure field and thus affect the heating-rate distribution. The $\varphi = 0^\circ$ data are considered to have the least interference problems between the sting and the flow; along this meridian $\dot{q}/\dot{q}_{s_{\alpha=0}}$ is 0.01 which is near the average of the data taken.

Flow visualization.- Oil flow patterns were used to indicate qualitatively regions of attached and separated flow over the afterbody. At angles of attack below 23° the oil drops on the afterbody surface did not move, indicating the afterbody flow was separated. At $\alpha = 23^\circ$, the oil drops near the meridian angle $\varphi = 0^\circ$ moved in the streamwise direction, indicating that afterbody flow attachment was beginning to occur. At $\alpha = 33^\circ$ the patterns showed the flow over most of the windward surface (approximately $\varphi = \pm 80^\circ$) was attached, while the flow over the leeward surface was separated. This latter pattern is shown in figure 8(a). (After the heat-transfer tests the model was disassembled and during reassembly for the flow visualization tests some of the fastening screws were not tightened against the surface and they protruded slightly as seen in figure 8(a). Since the Reynolds number of the present tests is quite low, the protrusions probably caused only local disturbances and, consequently, should not have altered the flow patterns from those that occurred during the pressure and heat-transfer tests.)

The wake flow pattern at $\alpha = 0^\circ$, obtained from the free-flight test, is shown in figure 8(b). The model and flow region are outlined because reproduction of the original photographs made some regions difficult to see. The luminescent grease vapors can be seen trailing behind the model and closing in the wave neck region less than 1 body diameter behind the model. These vapors are assumed to define the mixing region between the inviscid flow and the separated flow. The inner line can be thought of as a dividing line between the recirculating flow in the wake and the external flow which comes around the model. It is difficult to determine the direction of the flow

[redacted]

above the model surface from this photograph, but the average angle between the dividing line and the free-stream direction is estimated to be about -10°.

Comparisons With Other Data and Theory

The present pressure data for $\alpha = 2.5^{\circ}$ and $\alpha = 33^{\circ}$ are compared in figure 9 with the sting-supported data from other facilities. Data taken in both air and helium are shown. Also shown are the wind-tunnel free-flight data in air and helium reported in reference 2 which tend to substantiate the sting-supported data. The present data agree reasonably well with the data taken in air but they are somewhat higher than the helium data.

To see whether the results of figure 9 can be predicted by theory consider first the afterbody pressures at $\alpha = 0^{\circ}$. In reference 5 it is shown that the Apollo afterbody pressure in helium is adequately predicted by Prandtl-Meyer theory provided the direction of the separated flow is known. Since in flight this direction is not known, a desirable method for predicting the afterbody pressures would be one that does not depend on a priori knowledge of the flow separation angle. Such a method was suggested by Chapman (ref. 6), and extended in reference 7, to account for the effects of initial boundary-layer thickness. The method requires knowledge of the free-stream conditions, surface pressure prior to flow separation, and the thermochemical state of the gas as it flows over the body. Details of the method and the flow model are presented in appendix A and predictions made with the method are shown in figure 9(a). The theory predicts lower pressures for helium, about the same intermediate pressures for ideal air or air with frozen chemistry and equilibrium vibration, and higher pressures for equilibrium air. It will be shown later that the calculation in which frozen chemistry was assumed is reasonable for the present test data and hence that the theory and data agree well. This theory predicts for enthalpies and pressures corresponding to peak heating during entry of the full-scale vehicle, that the afterbody pressure ratios are 0.023 and 0.018 for equilibrium and frozen chemistry assumptions, respectively. These are essentially the same values as those shown for air in figure 9(a). Thus, flow chemistry should be taken into account when afterbody pressures are considered. The angle of flow separation also varies depending upon the flow chemistry. The direction predicted for the present data was -6.5° which can be compared with the photograph of figure 8(b). In that figure the estimated angle was about -10°. The comparison is believed to be reasonable considering the difficulties of interpreting the actual angles in figure 8(b).

Next, consider the windward afterbody pressure for α near 33°. In reference 1 the afterbody pressures for $\alpha = 33^{\circ}$ and $\varphi = 0^{\circ}$ were correlated by blast-wave theory. (This theory predicts a pressure distribution similar to that on a blunt flat plate at $\alpha = 0^{\circ}$; when the Apollo configuration is at $\alpha = 33^{\circ}$, the $\varphi = 0^{\circ}$ meridian is parallel to the free stream.) Therefore, the pressure-distribution data are compared with solutions (perfect-gas blunt-body and characteristic solutions, $\gamma = 1.4$) of reference 8 for a blunt plate with the nose radius equal to the test model corner radius. The prescribed α for the plate was the angle between the test-model windward surface and the free stream. (See figs. 9(b) and 4(a), (b), (c).) The agreement between theory and data is reasonably good for $\alpha = 33^{\circ}$ (fig. 9(b)); however, the pressures

[redacted]

were overpredicted at $\alpha = 44^\circ$ and underpredicted at $\alpha = 23^\circ$ (figs. 4(a), (c)). Note that the constant γ used in the theory is applicable provided the chemical composition is fixed over the windward surface. This will be substantiated later in the report. This theory predicts a somewhat higher pressure for helium than for air.

The heating-rate data for $\alpha = 2.5^\circ$ and $\alpha = 33^\circ$ are compared with data from other facilities in figure 10. Some of the heat-transfer data was reported as $h/h_{s_{\alpha=0}}$ and so it was converted to the cold wall equivalent, $\dot{q}/\dot{q}_{s_{\alpha=0}}$, by the equation

$$\frac{\dot{q}}{\dot{q}_{s_{\alpha=0}}} = \frac{h}{h_{s_{\alpha=0}}} \frac{T_r}{T_t}$$

where T_r/T_t was assumed to be 0.85. There is relatively good agreement between the various data at $\alpha = 33^\circ$, but at $\alpha \approx 0^\circ$ the difference is as much as a factor of 5. Although the heat transfer ordinarily follows the trends of the pressures which compared rather well at $\alpha \approx 0^\circ$, the differences here are attributed to sting-support interference for the reasons presented above during the discussion of the heat-transfer data.

The heating rates for $\alpha = 33^\circ$ and $\varphi = 0$, predicted by the reference-enthalpy method described in reference 9, are compared with the data in figure 10(b). The same blunt-plate approximation used in the pressure prediction was assumed. The resulting heating rate was computed with the following equation

$$\dot{q}_w = \frac{0.332 Z^2 u_e \rho' \mu' (h_t - h_w)}{Pr'^{2/3} \left(\int_0^x Z^2 u_e \rho' \mu' \, dx \right)^{1/2}}$$

where

$$h' = 0.23 h_e + 0.19 h_r + 0.58 h_w$$

The primes refer to properties evaluated at reference enthalpy, h'. The flow properties at the boundary-layer edge were obtained from a finite reaction rate calculation described in more detail later. The magnitude of $\dot{q}_{s_{\alpha=0}}$ was computed separately by the method of reference 10. The predicted and measured heating-rate ratios are in good agreement as shown in figure 10(a).

Finite Reaction Rate Streamtube Calculations

A very useful way of describing qualitatively the flow chemistry over the afterbody is to examine the chemical reaction rates along a representative streamtube (see ref. 11). This was done for the model and test conditions of the present investigation and also for the full-scale Apollo for representative flight conditions. The gas model used is given in reference 12. The species considered were N_2, O_2, N, O, N^+, O^+, e^- and the dissociation reactions were modified to include the approximate effects of the NO reactions. When applicable, ionization was considered in equilibrium. Although results are given for $\alpha = 33^\circ$ only, calculations not included show that the conclusions regarding the flow chemistry over the most leeward side of the body apply equally well at $\alpha = 0^\circ$.

The method considers streamtubes which begin immediately behind the shock wave near the stagnation line and pass over the most windward and most leeward sides of the body (see fig. 11). The pressure along this streamtube is assumed to be the body surface pressure and the distance traveled by the fluid in the streamtube is assumed to be the same as the body surface distance. The air passes across the shock in an undissociated state and enters the streamtube with an initial velocity, u_2, and the continuity, momentum, energy, and reaction rate equations are solved along the streamtube. Wind-tunnel values of surface pressure were used, but differences in pressure similar to those shown in figure 9(a) did not significantly influence the predicted afterbody chemical state.

The calculations are described by the species number fractions $[X_i]$ and $[Y_i]$, the atomic and ionized species fractions, respectively. These range from 0, where no atomic or ionized species exist (i.e., molecular air), to 1.0 where the maximum number of these species exist. A quasi-equilibrium number fraction, $[X_i]_{qe}$, is also given. It represents the species concentration that would exist if the gas were in equilibrium at the specified pressure and local temperature given by the finite rate calculations. Hence, if X_i and $[X_i]_{qe}$ are equal, the species can be considered in equilibrium, whereas the difference between $[X_i]$ and $[X_i]_{qe}$ is a qualitative measure of the degree of nonequilibrium.

Results for the shock-tunnel test conditions are presented in figure 11 for both the windward and leeward streamtubes and, generally, the same comments apply to both. The atomic species of oxygen $[X_O]$ starts at 0, because no initial dissociation is assumed, and rapidly approaches the quasi-equilibrium value of oxygen $[X_O]_{qe}$. From this point, in the vicinity of the corner, the reactions proceed so slowly that $[X_O]$ may be considered frozen; $[X_N]$ starts at zero and reaches $[X_N]_{qe}$ rapidly, then decreases to zero along with $[X_N]_{qe}$ as a result of the NO reactions. Note that the large initial values for $[X_N]_{qe}$ and $[X_O]_{qe}$ result from the very high initial temperature in the streamtube because it is assumed there are no chemical reactions across the shock wave. Since the amount of $[X_N]$ is small compared to $[X_O]$, it is concluded that the flow in the streamtube is frozen over the afterbody. This conclusion is believed to apply to other streamtubes farther away from the body, suggesting that the inviscid flow over the afterbody is frozen. Calculations of the isentropic exponent γ for the chemically frozen flow on the leeward side of the body ranged from 1.35 for vibrations in equilibrium to 1.46 for the frozen vibrations. Thus, the isentropic exponent for the chemically frozen expansion

[redacted] DECLASSIFIED

was very similar to that for a perfect gas with $\gamma = 1.4$. This is a reasonable explanation of why the shock-tunnel pressure data agree with other wind-tunnel data for lower temperatures.

Next, the analysis was applied to a full-size vehicle for the maximum heating conditions of the overshoot, undershoot, and emergency trajectories and the results are presented in figures 12(a) through (f). The entry velocities were sufficiently high that ionization of the atoms occurred as indicated by $[Y_i]$. The gas flow achieved equilibrium rapidly as a result of the vehicle size. There was complete dissociation of O_2 and almost complete dissociation of the N_2. The temperatures were so high that even during the expansion around the corner of the vehicle, the oxygen was in equilibrium in a completely dissociated state. The recombinations for this case therefore concerned only the nitrogen reactions.

For the overshoot condition (figs. 12(a) and (b)) the air can be considered frozen during the expansion around the corner at a nearly fully dissociated level. (The increase in $[X_N + Y_N]_{qe}$ for the leeward streamline beyond the corner is caused by the increasing temperature resulting from recombination of X_N.) In this case, one would expect the afterbody pressures to correspond to those obtained in low enthalpy air wind-tunnel tests, since the isentropic exponents are essentially the same ($\gamma \approx 1.35$ compared to $\gamma = 1.4$).

The air in the streamtubes for the undershoot trajectory (figs. 12(c) and (d)) did not freeze at any fixed composition. The recombination reactions were just slow enough on the afterbody that the flow never achieved equilibrium after the expansion around the corner. It is difficult to predict what the afterbody pressures would be for this case, but they probably would lie between the values for an equilibrium expansion and the wind-tunnel data. See, for example, the trends indicated in figure 9(a).

The emergency trajectory (figs. 12(e) and (f)) had the maximum heating point at a considerably lower altitude than the overshoot condition so the density was an order of magnitude higher. The increased density produced chemical recombinations that were sufficiently rapid to bring the flow to equilibrium for most of the afterbody length, the exception being near the corner. Again, these results indicate that afterbody pressures would be between the values for an equilibrium expansion and the wind-tunnel data.

CONCLUSIONS

Shock-tunnel tests of the Apollo afterbody pressure and heat transfer along with study of the flow chemistry resulted in the following conclusions.

1. Pressure, heat-transfer, and flow visualization data showed that the flow is separated from the afterbody at $\alpha = 0^\circ$, attaches on the windward meridian ($\varphi = 0^\circ$) near $\alpha = 23^\circ$, and remains attached over most of the windward surface ($\varphi = \pm 80^\circ$) for $\alpha \geq 33^\circ$.

[redacted]

2. Pressure and heating-rate distributions on the windward surface at $\alpha = 33^\circ$ were adequately predicted by a blunt-plate approximation; at $\alpha = 44^\circ$ and 23° this two-dimensional theory was not adequate; at $\alpha = 0^\circ$ the afterbody pressures were predicted by a method which did not depend on a priori knowledge of the flow separation direction.

3. Analysis of the flow chemistry along a representative streamtube showed the inviscid flow over the afterbody was probably frozen for the shock-tunnel test conditions. For selected flight conditions of a full-size vehicle, the results showed that at peak heating, either frozen or equilibrium inviscid afterbody flow can be expected depending on the trajectory considered.

Ames Research Center
National Aeronautics and Space Administration
Moffett Field, Calif., Oct. 12, 1965

[redacted]

APPENDIX A

AFTERBODY PRESSURE PREDICTION METHOD

A method is presented for predicting the Apollo afterbody pressure in the separated region at hypersonic speeds. The general method follows that of reference 7 which is here modified to apply specifically to the Apollo configuration. The method requires knowledge of the free-stream conditions and pressure distribution prior to flow separation. It can be utilized to estimate separated pressures on the Apollo afterbody for flight conditions, and the separation angle predicted can be used to define an inner boundary for characteristic solutions for the inviscid flow over the afterbody.

The flow model is shown in sketch (a). The base flow region extends from the corner of the body to the wake neck. The presence of the afterbody is assumed to have no influence on the base flow. The separated boundary layer begins with a finite thickness due to the upstream flow over the body. The fluid in the boundary layer flows around the corner and mixes with the relatively slower and reversed flow in the base region. A nonsimilar velocity and enthalpy distribution in the boundary layer ensues from the point of separation as a result of this mixing and gradually approaches the fully developed similar velocity distribution considered by Chapman in reference 13. A dividing streamline separates the streamlines which continue downstream through the wake neck from those that recirculate. The total pressure along the dividing streamline is assumed to be the static pressure downstream of the wake neck. No static pressure gradient is accounted for in the wake neck. The inviscid flow is assumed to follow a Prandtl-Meyer expansion from a sonic point on the

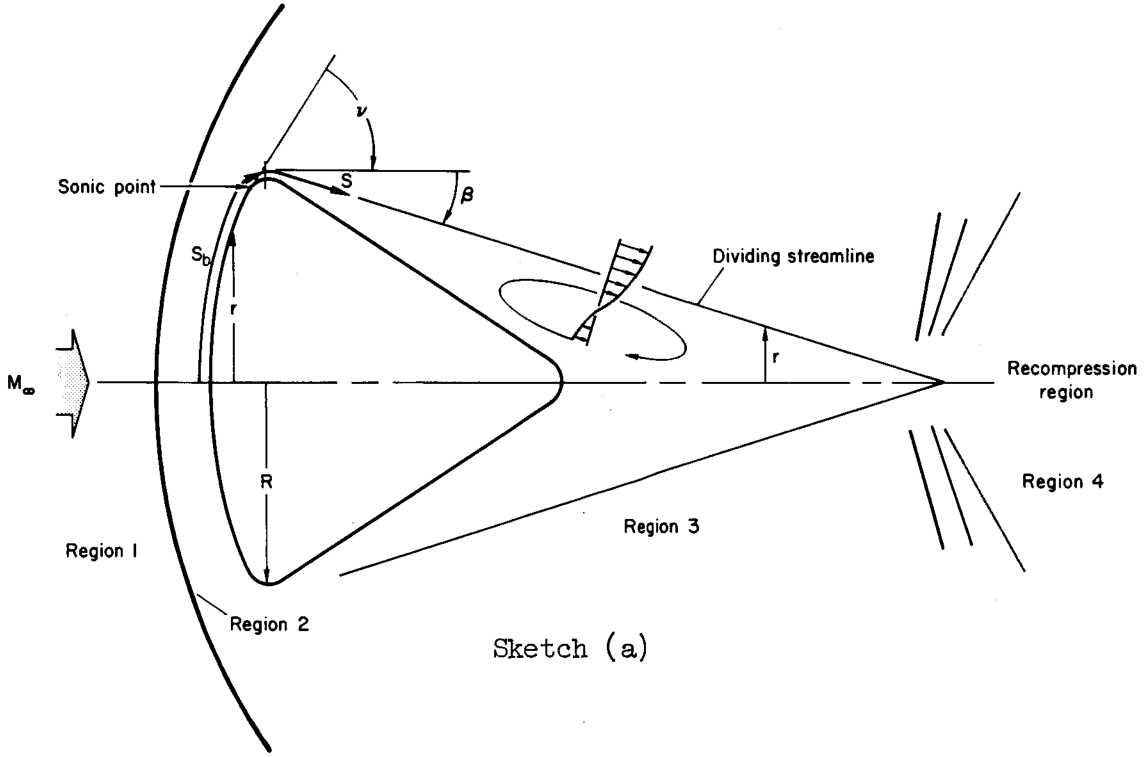

Sketch (a)

forebody surface to the flow-separation direction given by the dividing streamline. At the wake neck an isentropic recompression region is assumed to turn the flow in a direction parallel to the free-stream direction.

The solutions presented in reference 7 for the nonsimilar boundary-layer equations are coupled to the inviscid flow through the conditions at the boundary-layer outer edge and the assumption regarding the total pressure along the dividing streamline mentioned above. The solutions are in terms of two dependent variables u^*, the dimensionless dividing streamline velocity u_d/u_e, and S^*, the dimensionless distance from the onset of separation.

For axisymmetric bodies S^* may be written as

$$S^* = \frac{\displaystyle\int_{S_b}^{S} \left(\frac{\rho_e}{\rho_{t_2}}\right)\left(\frac{u_e}{u_\infty}\right)\left(\frac{\mu_e}{\mu_{t_2}}\right) r^2\, dS}{\displaystyle\int_{0}^{S_b} \left(\frac{\rho_e}{\rho_{t_2}}\right)\left(\frac{u_e}{u_\infty}\right)\left(\frac{\mu_e}{\mu_{t_2}}\right) r^2\, dS} \tag{A1}$$

and it represents the transformed distance along the dividing streamline normalized by the transformed distance along the forebody surface. The normalized dividing streamline velocity, u^*, varies from 0 at the start of separation to 0.587 (Chapman's value for the fully developed separated velocity profile) at $S^* = \infty$. The value of u^* depends on the conditions at the outer edge of the separated boundary layer, the distance from the separation point, and the static pressure downstream of the wake neck. It can be related to the outer edge conditions by the following equation taken from reference 7

$$\frac{p_4}{p_e} = \left[1 + \frac{\frac{\gamma - 1}{2} u^* M_e^2}{1 + \frac{\gamma - 1}{2} M_e^2 (1 - u^{*2}) - \left(1 + \frac{\gamma - 1}{2} M_e^2\right)\left(1 - \frac{H_w}{H_e}\right)\Omega(S^*)}\right] \tag{A2}$$

where $\Omega(S^*)$ accounts for the temperature or enthalpy of the separated region and may be obtained from reference 7. Equation (A2) is applicable to real gases, provided the value of γ is assumed constant from the streamline of the boundary layer outer edge to the dividing streamline, or a suitable average value of γ between these streamlines is assumed.

Before relating the specific steps in the method, it is worthwhile to rewrite equation (1) in a form directly applicable to the Apollo vehicle. If the value of the isentropic exponent is assumed to be constant over the forebody and afterbody (not necessarily the same numerical value) and a viscosity law to be of the form $\mu \sim T^{\omega}$, equation (1) becomes

$$S^* = \frac{\displaystyle\int_{S_b}^{S} \left(\frac{p_e}{p_{t_2}}\right)^{\omega+\frac{1-\omega}{\gamma}} \left[1 - \left(\frac{p_e}{p_{t_2}}\right)^{\frac{\gamma-1}{\gamma}}\right]^{1/2} r^2\, dS}{\displaystyle\int_{0}^{S_b} \left(\frac{p_e}{p_{t_2}}\right)^{\omega+\frac{1-\omega}{\gamma}} \left[1 - \left(\frac{p_e}{p_{t_2}}\right)^{\frac{\gamma-1}{\gamma}}\right]^{1/2} r^2\, dS} \tag{A3}$$

For a constant pressure (p_e) in the afterbody region and for a straight dividing streamline, equation (A3) may be integrated over the entire dividing streamline and rewritten

$$S^* = \frac{\displaystyle \left(\frac{p_e}{p_{t_2}}\right)^{\omega+\frac{1-\omega}{\gamma}} \left[1 - \left(\frac{p_e}{p_{t_2}}\right)^{\frac{\gamma-1}{\gamma}}\right]^{1/2} \frac{R^3}{3 \sin \beta}}{\displaystyle\int_{0}^{S_b} \left(\frac{p_e}{p_{t_2}}\right)^{\omega+\frac{1-\omega}{\gamma}} \left[1 - \left(\frac{p_e}{p_{t_2}}\right)^{\frac{\gamma-1}{\gamma}}\right]^{1/2} r^2\, dS} \tag{A4}$$

The denominator of equation (A4) was discussed in reference 4 wherein it was found that for the Apollo at $\alpha = 0^\circ$ the pressure distribution over the forebody was essentially independent of gas composition and that the integral depended mostly on γ. The inverse value of this integral multiplied by R^3 is plotted for various γ in figure 13. The forebody pressure distribution used is that of reference 4.

Equations (A2) and (A4) along with assumptions regarding the inviscid flow are adequate for calculating the afterbody pressure. As mentioned earlier, a Prandtl-Meyer expansion around the corner radius and a Prandtl-Meyer recompression downstream of the wake neck are assumed. The procedure is to assume a direction for the separated flow (i.e., the angle β in sketch (a)) and determine the Prandtl-Meyer turning angle between the sonic point (located, e.g., by the method in ref. 14) and the assumed direction to obtain the outer-edge boundary-layer conditions. Then the ratio p_4/p_e is obtained by the Prandtl-Meyer recompression at the neck. From the assumed conditions at the outer edge of the boundary layer S^* is calculated and the values of u^* and $\Omega(S^*)$ are taken from reference 7 and equation (A2) is solved for p_4/p_e. This value is compared to the ratio p_e/p_4 from the inviscid flow and an iteration is carried out until the two values for p_e/p_4 are matched.

It is interesting to note that this method can be readily adapted for an ablating forebody. One still uses equations (A2) and (A4) along with the

[redacted]

assumption of Prandtl-Meyer turning, but the values of u^* and $\Omega(S^*)$ are altered to account for blowing. These are tabulated in reference 15 as a function of S^*. As shown in reference 15, a rise in afterbody pressure with increased blowing would be expected and the rise would probably not exceed 25 percent.

[redacted]

REFERENCES

1. Lee, George; and Sundell, Robert E.: Heat-Transfer and Pressure Distributions on Apollo Models at $M = 13.8$ in an Arc-Heated Wind Tunnel. NASA TM X-1069, 1965.

2. Kemp, Joseph H., Jr.: Telemetry Measurements of Afterbody Pressures on Free Flying Models of the Apollo Capsule at Mach Numbers From 10 to 21 in Helium and 14 in Air. NASA TM X-1154, 1965.

3. Cunningham, Bernard E.; and Kraus, Samuel: A 1-Foot Hypervelocity Shock Tunnel in Which High-Enthalpy, Real-Gas Air Flows can be Generated With Flow Times of About 180 Milliseconds. NASA TN D-1428, 1962.

4. Marvin, Joseph G; Tendeland, Thorval; and Kussoy, Marvin: Apollo Forebody Pressure and Heat-Transfer Distributions in Helium at $M_\infty = 20$. NASA TM X-854, 1963.

5. Marvin, Joseph G.; and Kussoy, Marvin: Experimental Investigation of the Flow Field and Heat Transfer Over the Apollo-Capsule Afterbody at a Mach Number of 20. NASA TM X-1032, 1965.

6. Chapman, Dean R.; Kuehn, Donald M.; and Larson, Howard K.: Investigation of Separated Flows in Supersonic and Subsonic Streams With Emphasis on the Effect of Transition. NACA Rep. 1356, 1958.

7. King, H. H.; and Baum, E.: Enthalpy and Atom Profiles in the Laminar Separated Shear Layer. EOS-RN 8, March 1963.

8. Cleary, Joseph W.; and Axelson, John A.: Theoretical Aerodynamic Characteristics of Sharp and Circularly Blunt-Wedge Airfoils. NASA TR R-202, 1964.

9. Nielsen, J. N.; Goodwin, F. K.; Sacks, A. H.; Burnell, J. A.; and Rubesin, M. W.: Effects of Supersonic and Hypersonic Aircraft Speed Upon Aerial Photography. Vidya Rep. 28, Oct. 1960.

10. Fay, J. A.; and Riddell, F. R.: Theory of Stagnation Point Heat Transfer in Dissociated Air. J. Aero. Sci., vol. 25, no. 2, Feb. 1958, pp. 73-85 and 121.

11. Heims, S. P.: Effect of Oxygen Recombination on One-Dimensional Flow at High Mach Numbers. NACA TN 4144, 1958.

12. Reinhardt, Walter A.; and Baldwin, Barrett S., Jr.: A Model for Chemically Reacting Nitrogen-Oxygen Mixtures With Application to Nonequilibrium Air Flow. NASA TN D-2971, 1965.

13. Chapman, Dean R.: Laminar Mixing of a Compressible Fluid. NACA Rep. 958, 1950.

14. Kaattari, George E.: Shock Envelopes of Blunt Bodies at Large Angles of Attack. NASA TN D-1980, 1963.

15. Baum, E.: Effect of Boundary Layer Blowing on the Laminar Separated Shear Layer. EOS-RN 9, April 1963.

[redacted]LASSIFIED

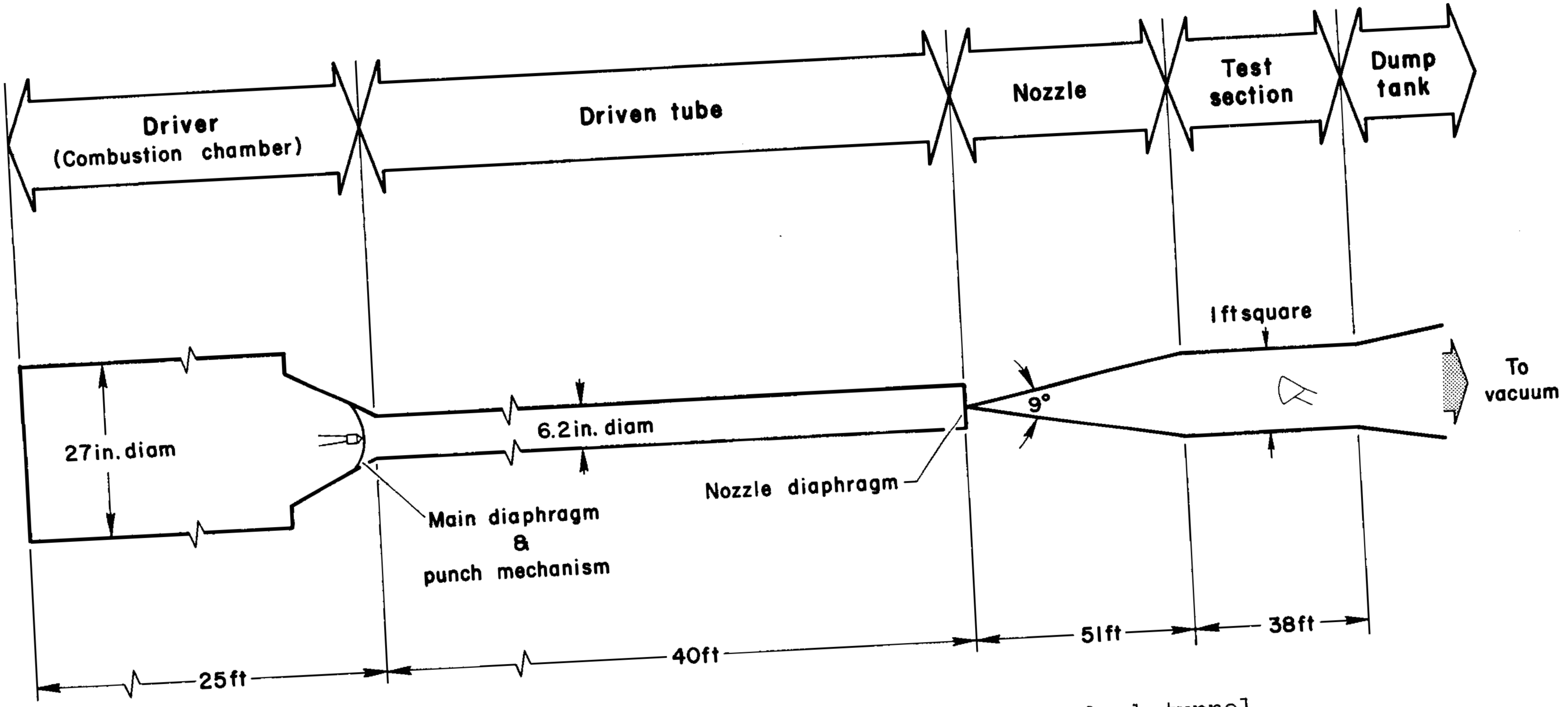
Driver
(Combustion chamber)
Driven tube
Nozzle
Test section
Dump tank
To vacuum
27in. diam
6.2in. diam
Main diaphragm & punch mechanism
Nozzle diaphragm
9°
1ft square
25ft
40ft
51ft
38ft

Figure 1.- Schematic drawing of the Ames 1-foot shock tunnel.

[redacted]

UNCLASSIFIED

[redacted]

[redacted]

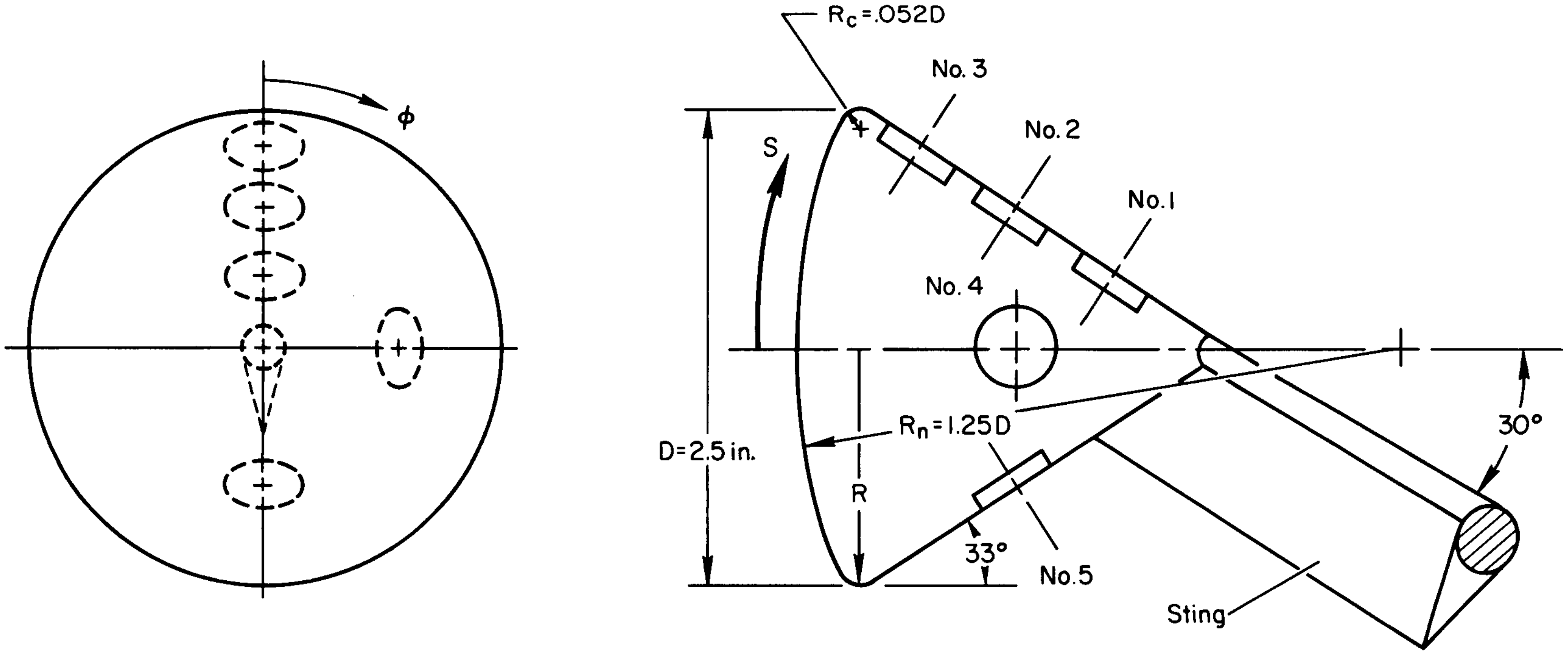
ϕ
$R_c = .052D$
No. 3
No. 2
No. 1
No. 4
S
D=2.5 in.
$R_n = 1.25D$
R
33°
No. 5
30°
Sting

Cell no.	S/R	ϕ
1	2.356	0°
2	1.868	0°
3	1.380	0°
4	1.868	90°
5	1.868	180°

(a) Cell location.

Figure 2. - Pressure model.

D [redacted] LASSIFIED

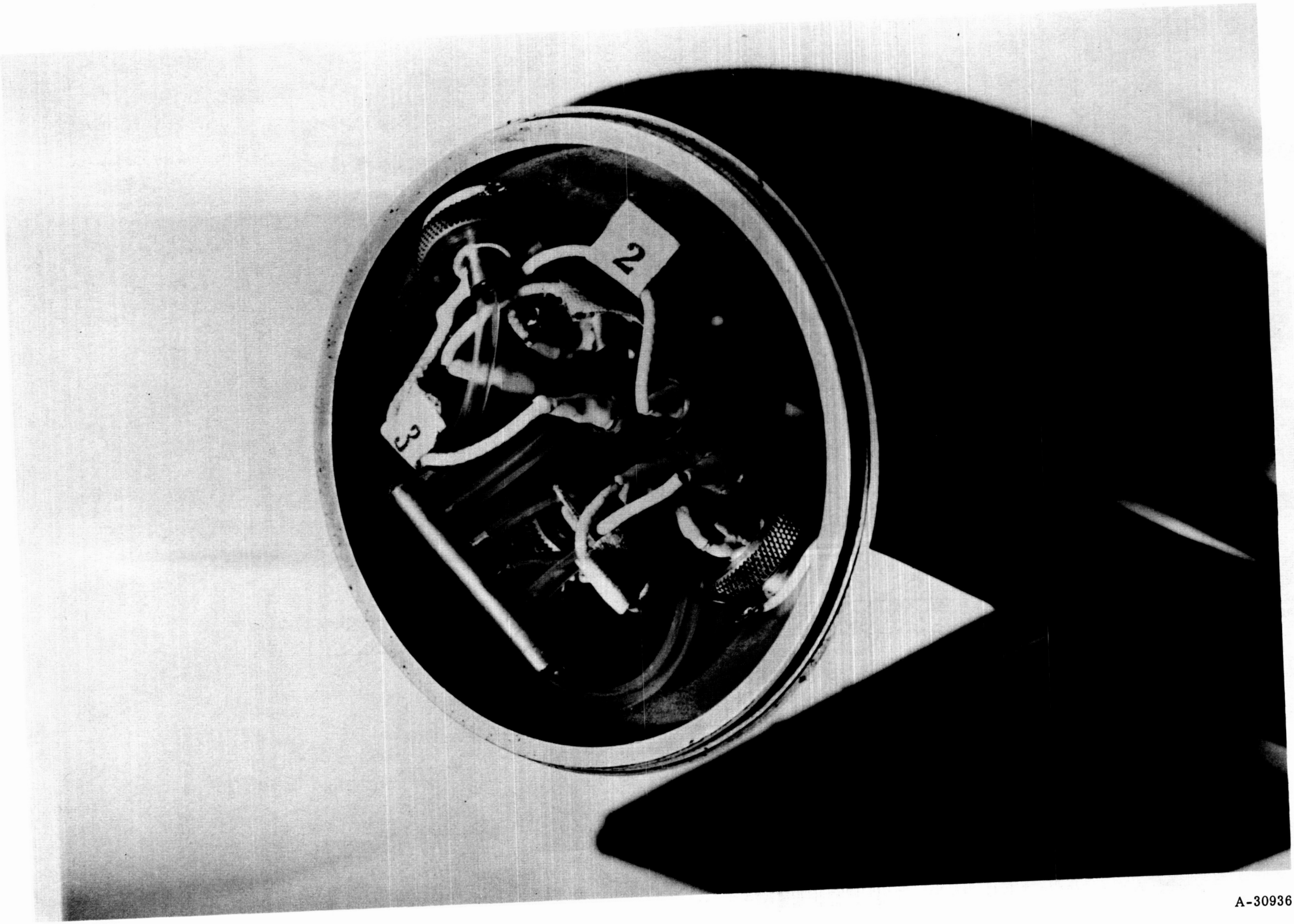

A-30936

(b) Cell installation.

Figure 2.- Continued.

[redacted]

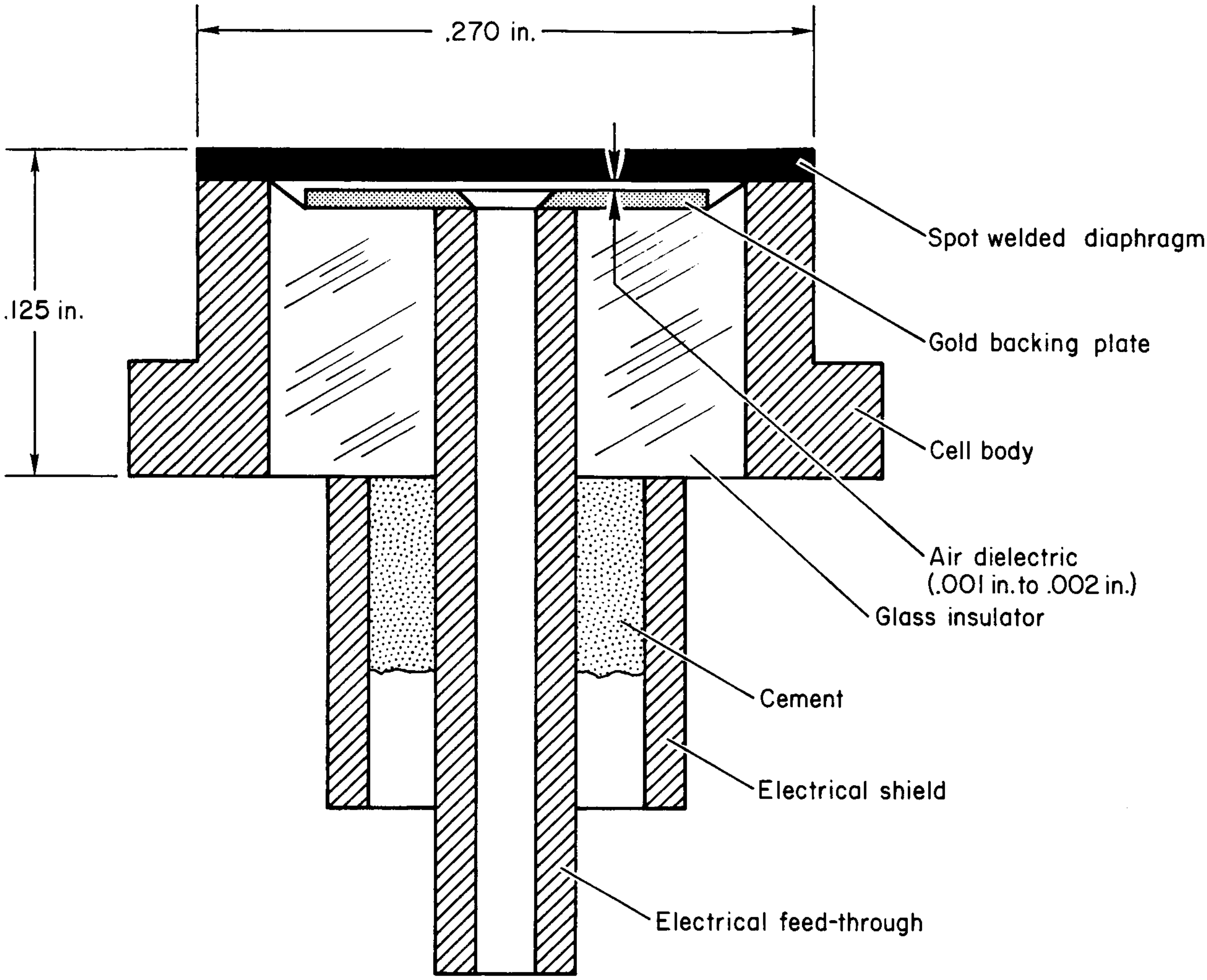
.270 in.
.125 in.
Spot welded diaphragm
Gold backing plate
Cell body
Air dielectric
(.001 in. to .002 in.)
Glass insulator
Cement
Electrical shield
Electrical feed-through

(c) Schematic diagram of transducer.

Figure 2.- Concluded.

[redacted]LASSIFIED

TC no.	S/R	ϕ
1	1.455	0°
2	1.611	
3	1.768	
4	1.924	
5	2.080	
6	2.237	
7	2.393	
8	1.455	45°
9	1.768	
10	2.080	
11	2.393	
12	1.455	90°
13	1.768	
14	2.080	
15	2.393	
16	1.455	180°
17	1.768	
18	2.080	

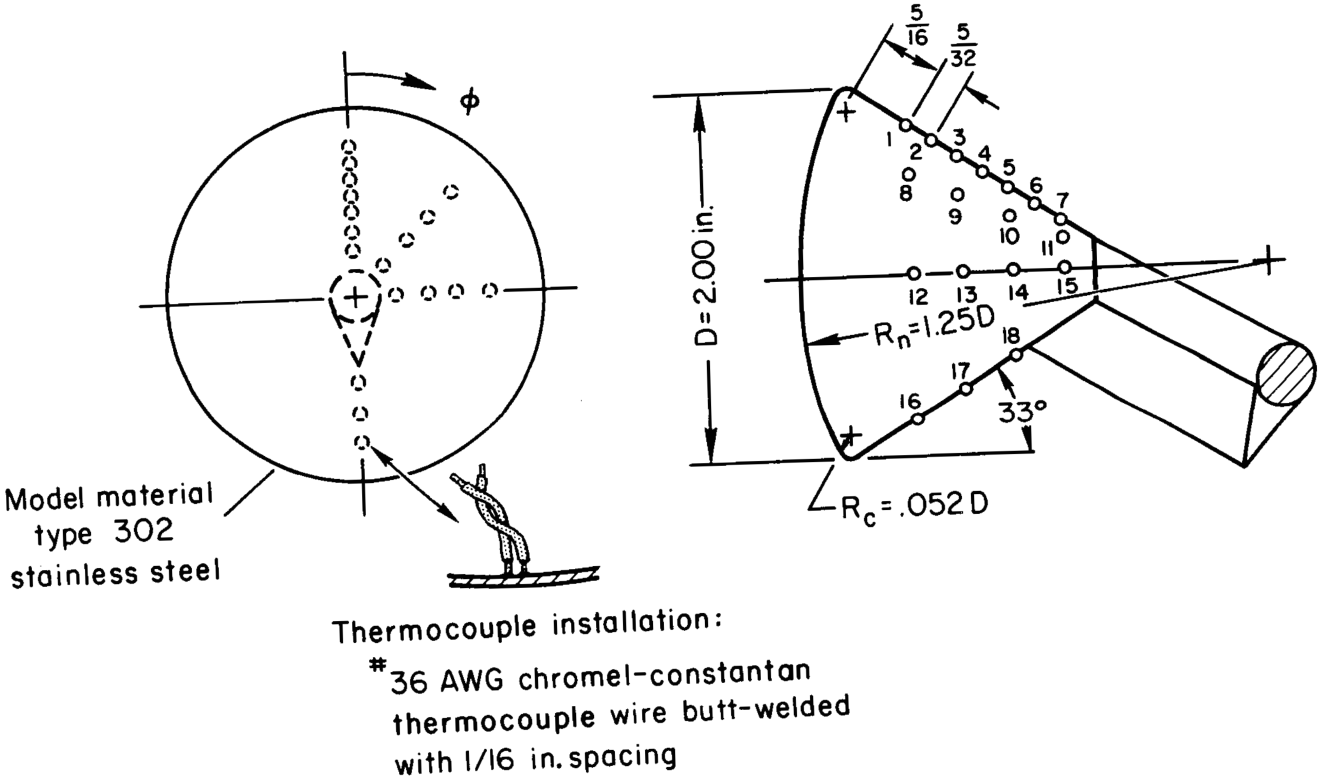
ϕ
Model material
type 302
stainless steel
Thermocouple installation:
#36 AWG chromel-constantan
thermocouple wire butt-welded
with 1/16 in. spacing
$\frac{5}{16}$
$\frac{5}{32}$
1
2
3
4
5
6
7
8
9
10
11
12
13
14
15
16
17
18
D = 2.00 in.
$R_n = 1.25D$
$R_c = .052D$
33°

Figure 3.- Heat-transfer model.

[redacted]

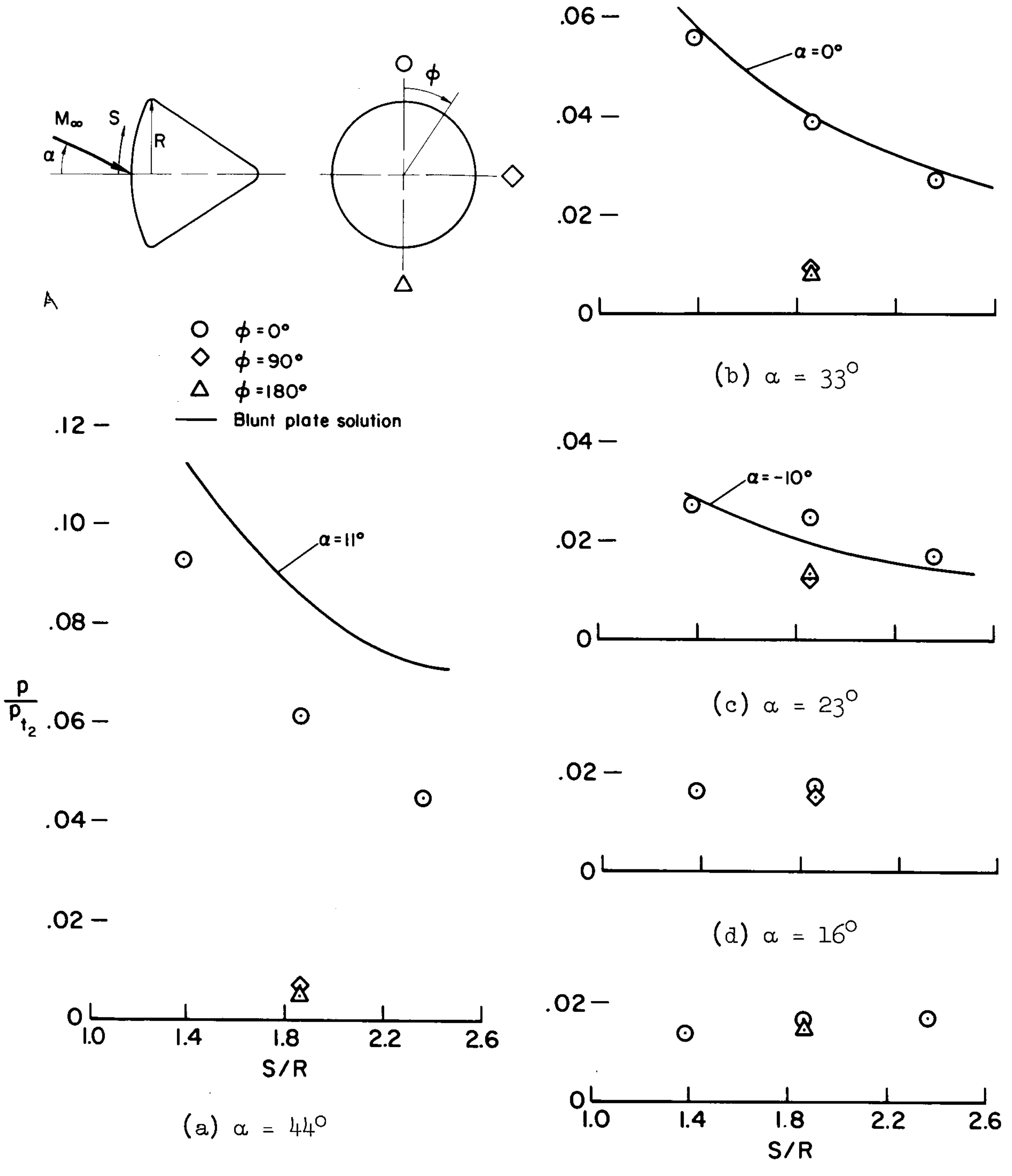

(a) $\alpha = 44^\circ$

(b) $\alpha = 33^\circ$

(c) $\alpha = 23^\circ$

(d) $\alpha = 16^\circ$

(e) $\alpha = 2.5^\circ$

Figure 4.- Afterbody pressure distribution.

[redacted]

[redacted]LASSIFIED

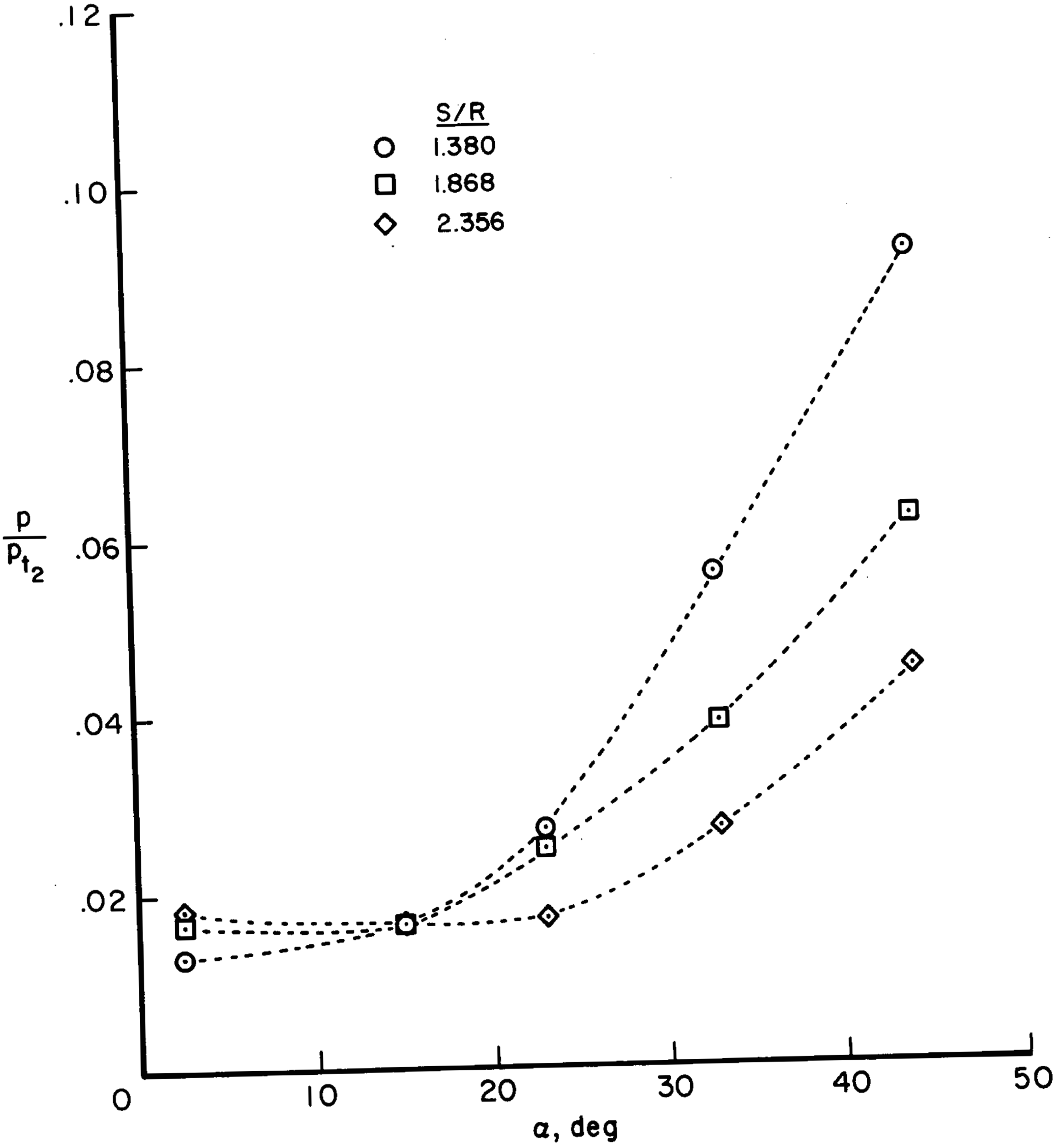

Figure 5.- Variation with α of the afterbody pressure ratio on the most windward ray.

[redacted]

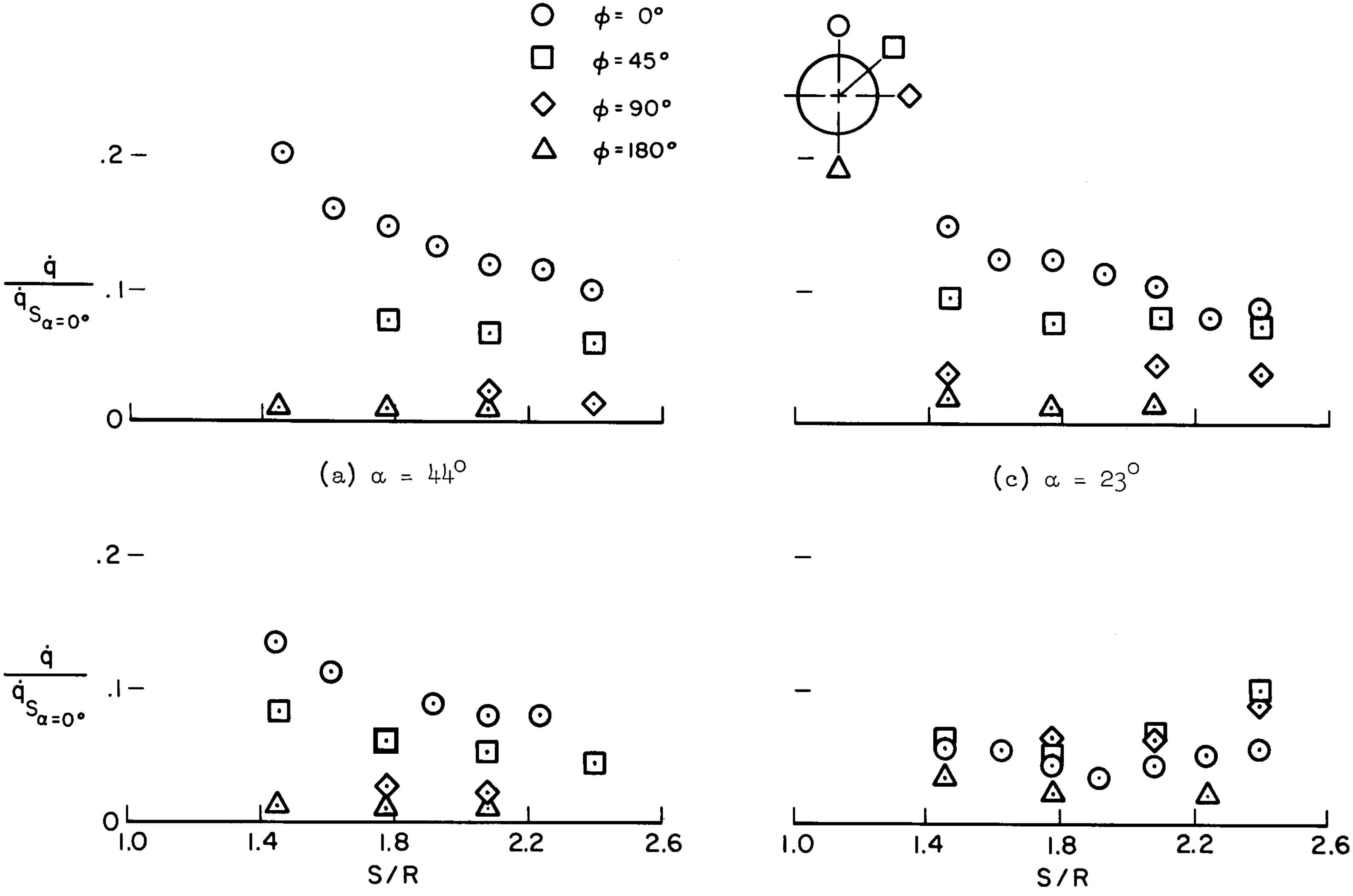

(a) $\alpha = 44°$

(c) $\alpha = 23°$

(b) $\alpha = 33°$

(d) $\alpha = 2.5°$

Figure 6.- Normalized afterbody heat transfer.

[redacted]

DECLASSIFIED

[redacted]

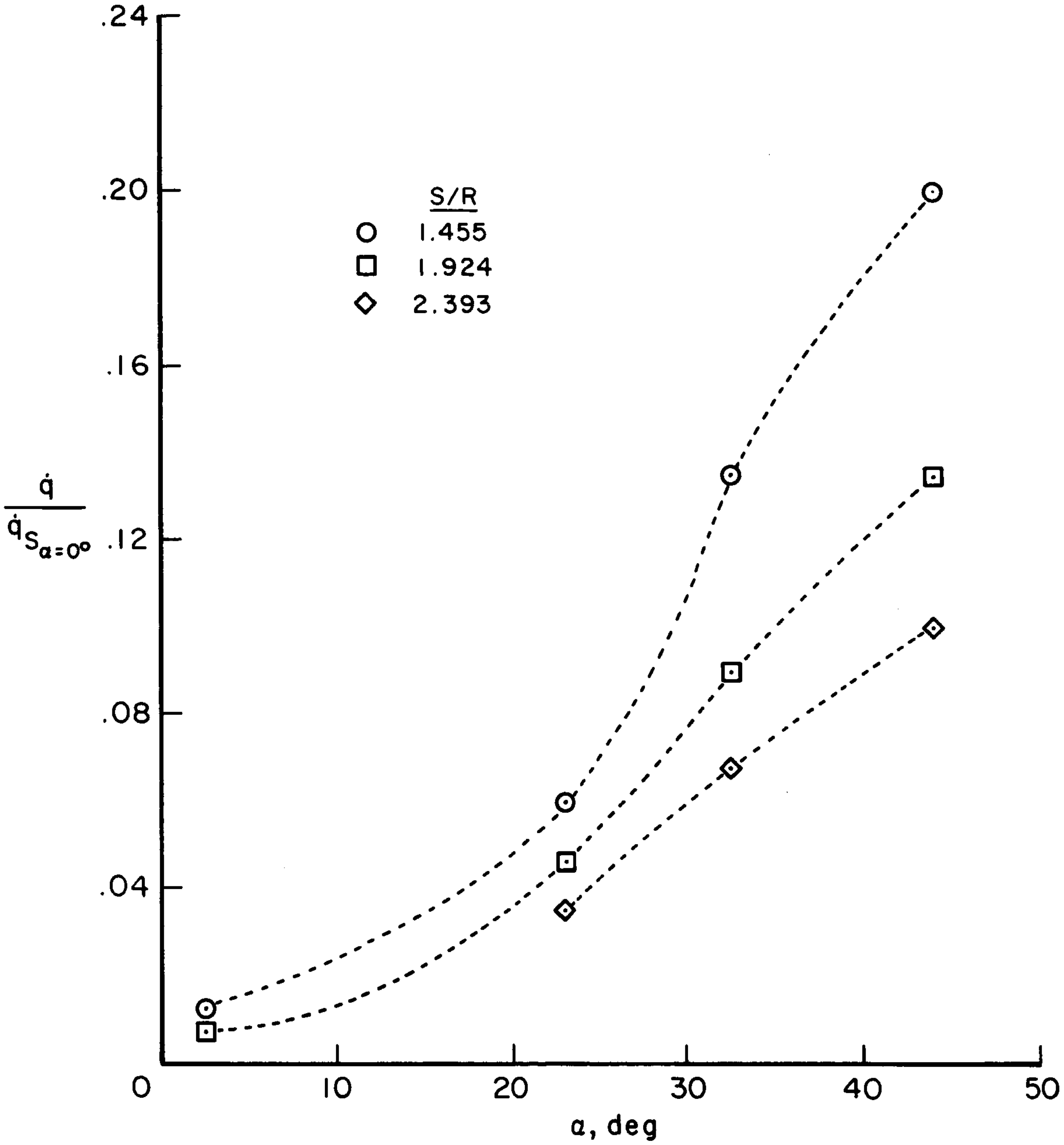

Figure 7.- Variation with α of the afterbody heating-rate ratio on the most windward ray.

[redacted]

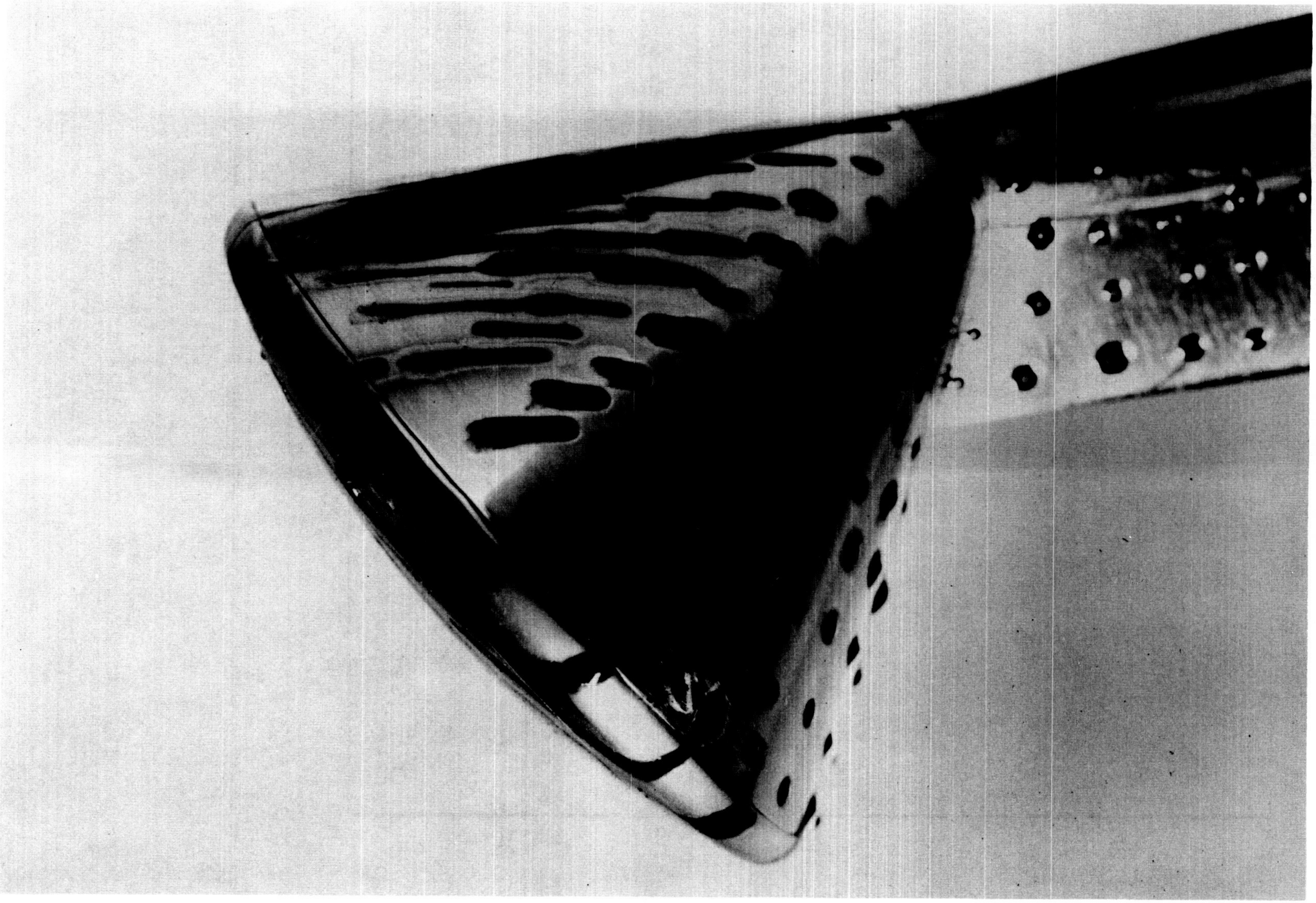

A-30476

(a) Oil-dot flow pattern, $\alpha = 33^\circ$.

Figure 8.- Flow visualization results.

[redacted]

DE[redacted]SSIFIED

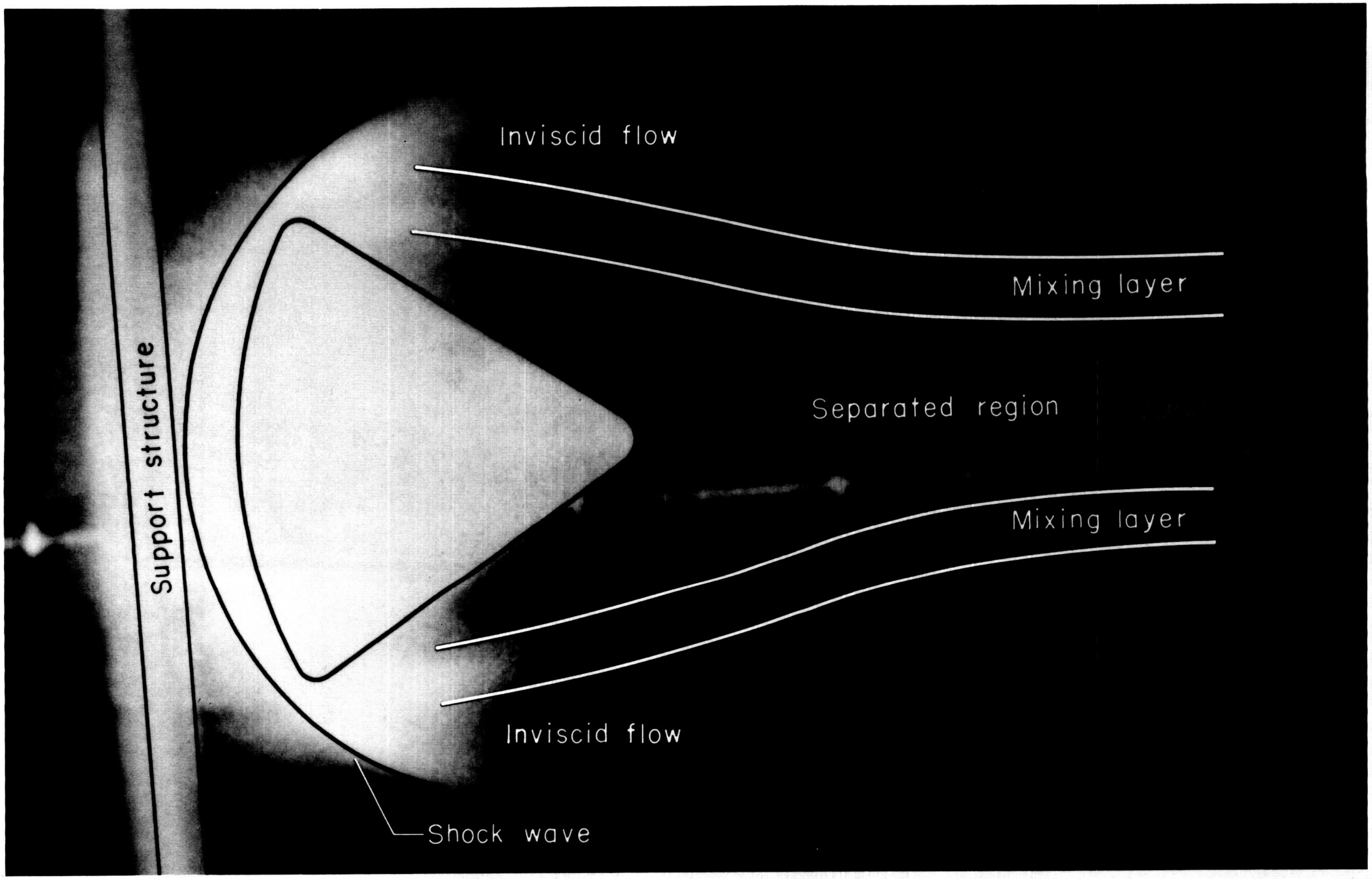
Inviscid flow
Mixing layer
Separated region
Mixing layer
Inviscid flow
Support structure
Shock wave

A-31391

(b) Wake flow pattern, $\alpha = 0^\circ$.

Figure 8.- Concluded.

[redacted]

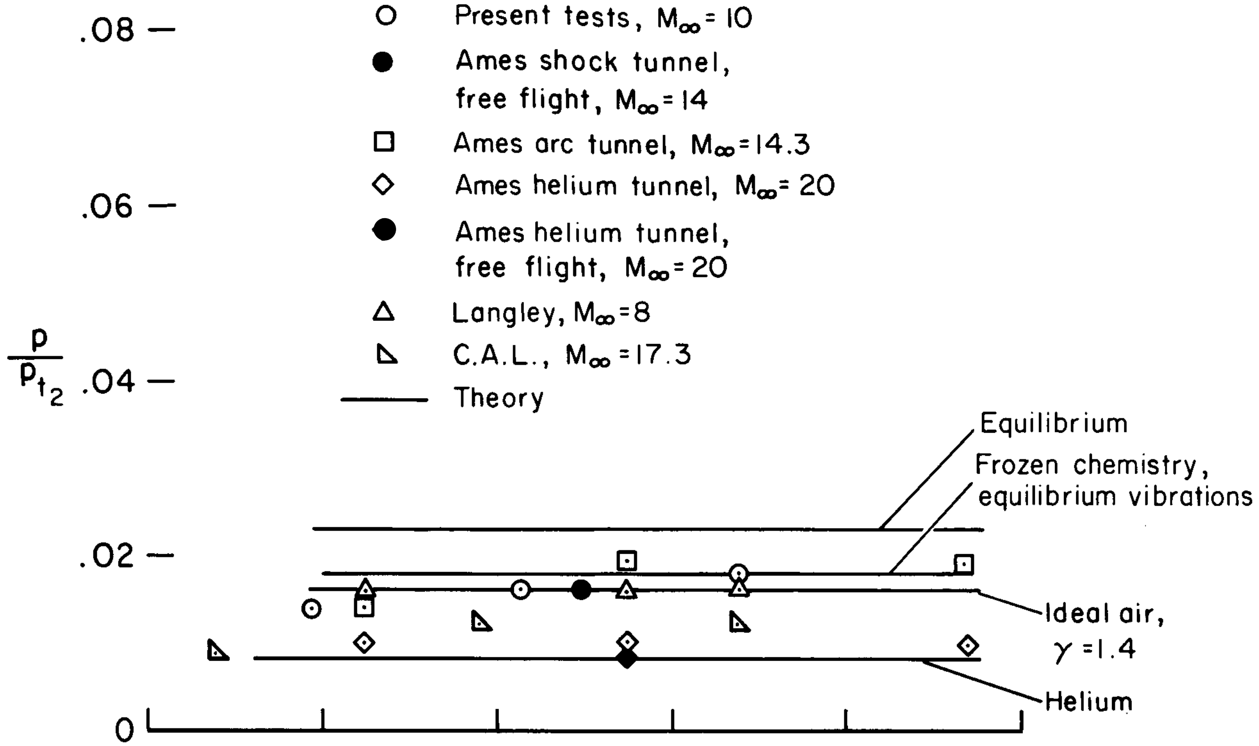

(a) $\alpha = 0^\circ$

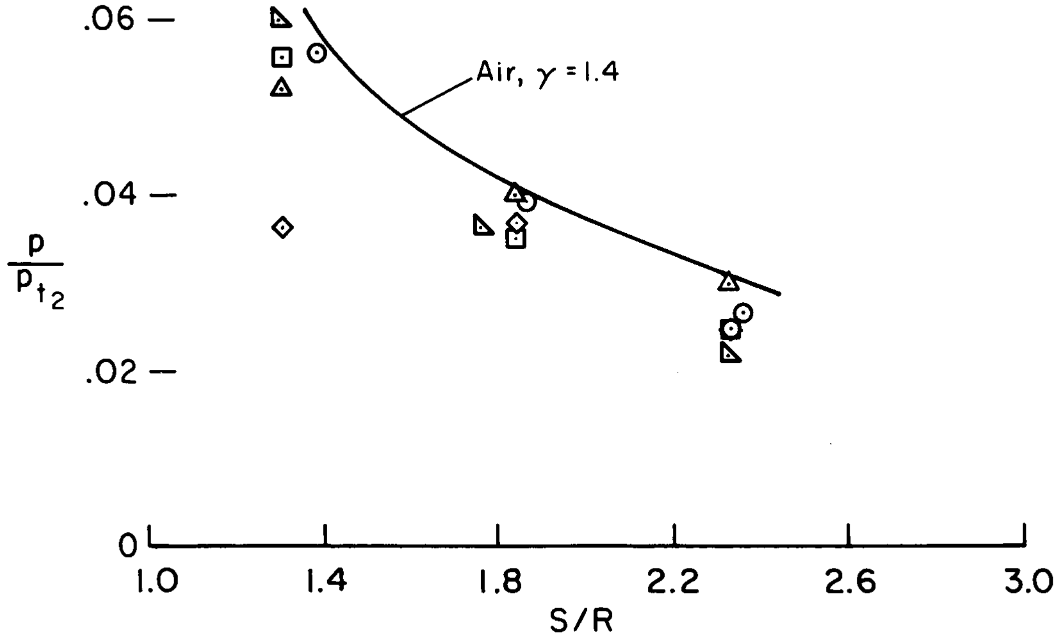

(b) $\alpha = 33^\circ$

Figure 9.- Comparison of Apollo afterbody pressure data from various sources.

[redacted]

DECLASSIFIED

[redacted]

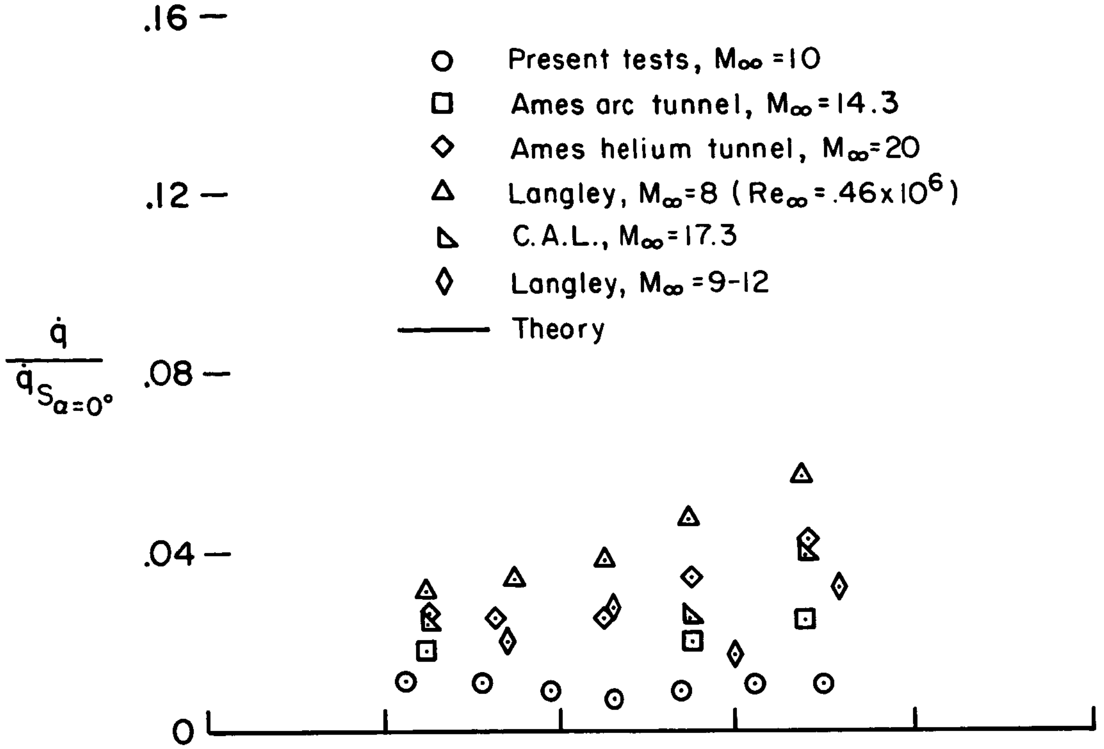

(a) $\alpha = 0^\circ$

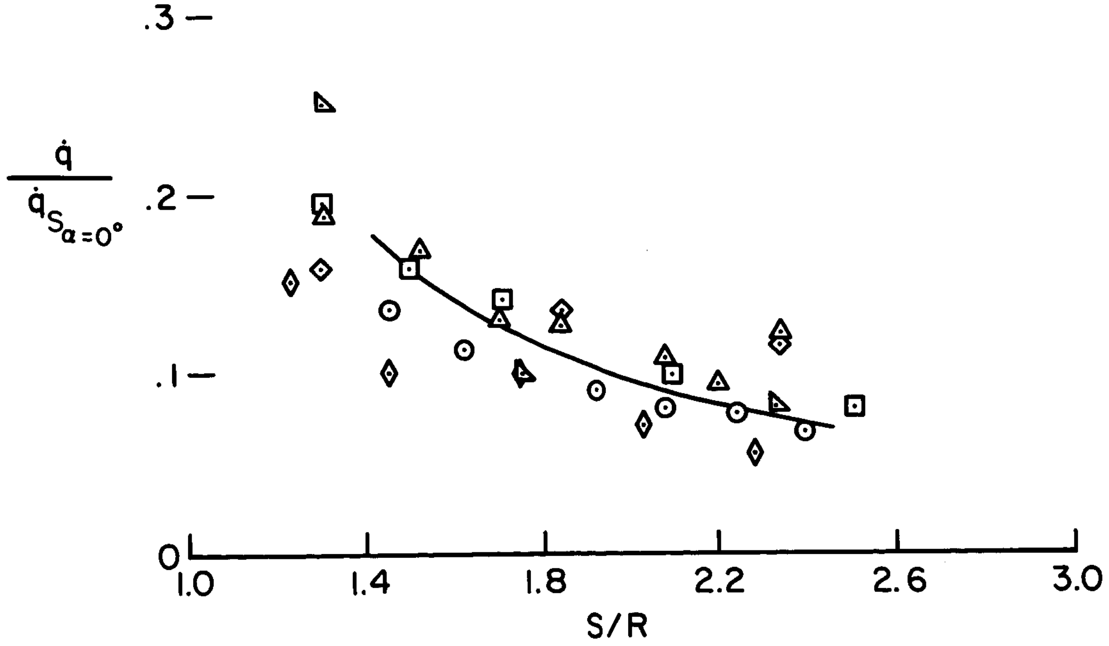

(b) $\alpha = 33^\circ$

Figure 10.- Comparison of Apollo afterbody heating-rate ratio data from various sources.

[redacted]

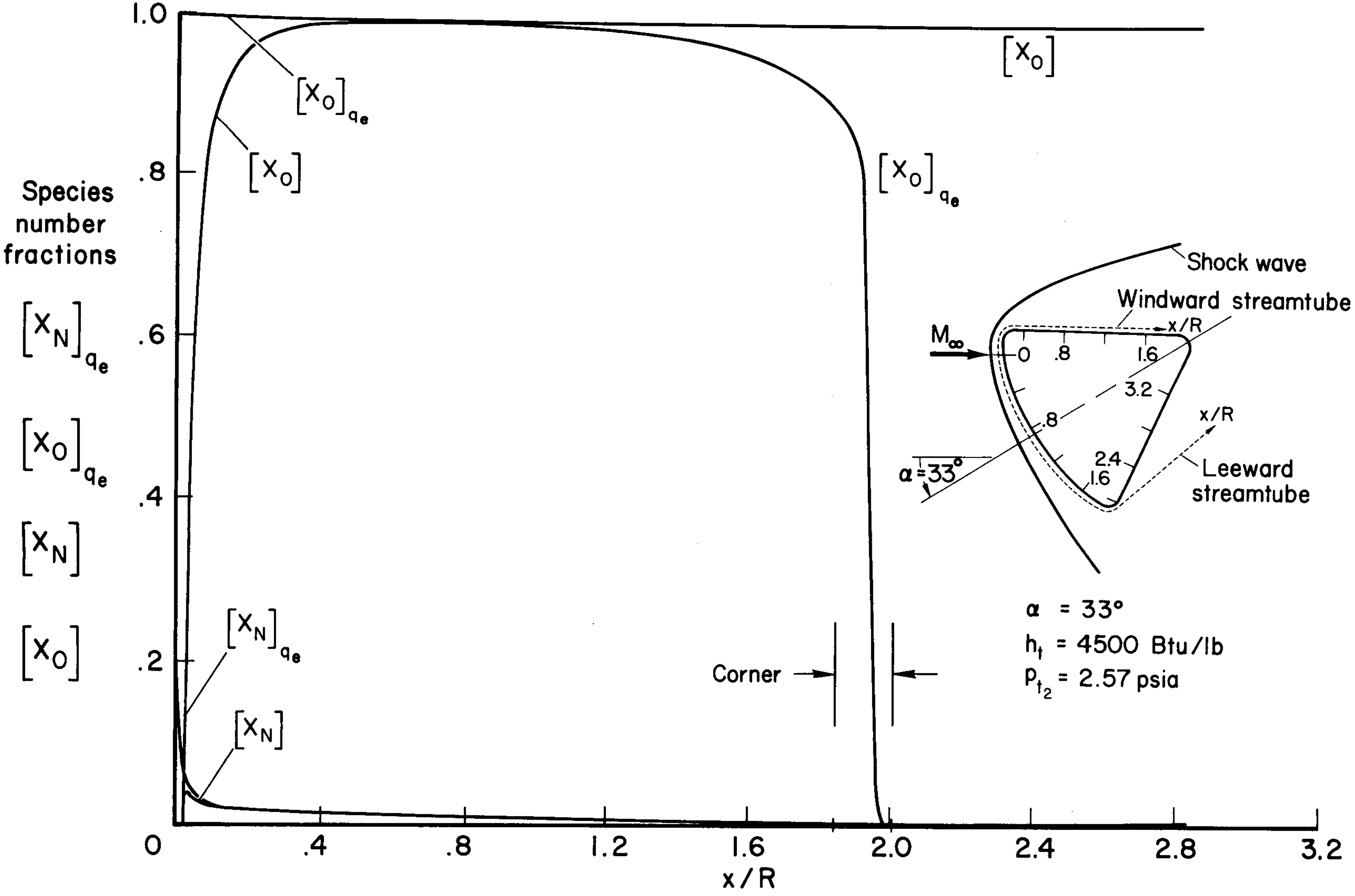

(a) Leeward side.

Figure 11.- Species fractions along a streamtube close to the surface of the test model for the present test conditions.

[redacted]

DECLASSIFIED

[redacted]

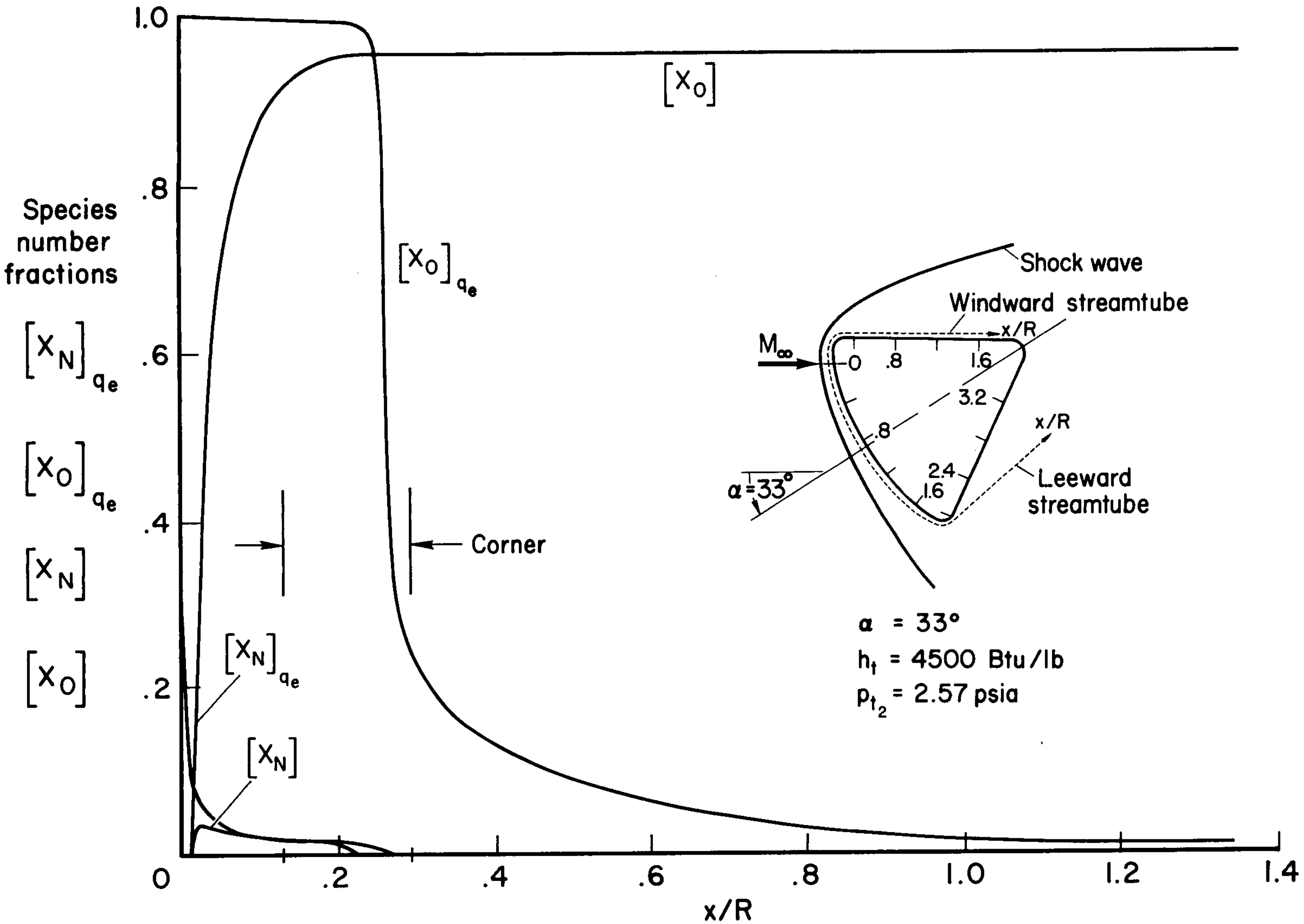

(b) Windward side.

Figure 11.- Concluded.

[redacted]

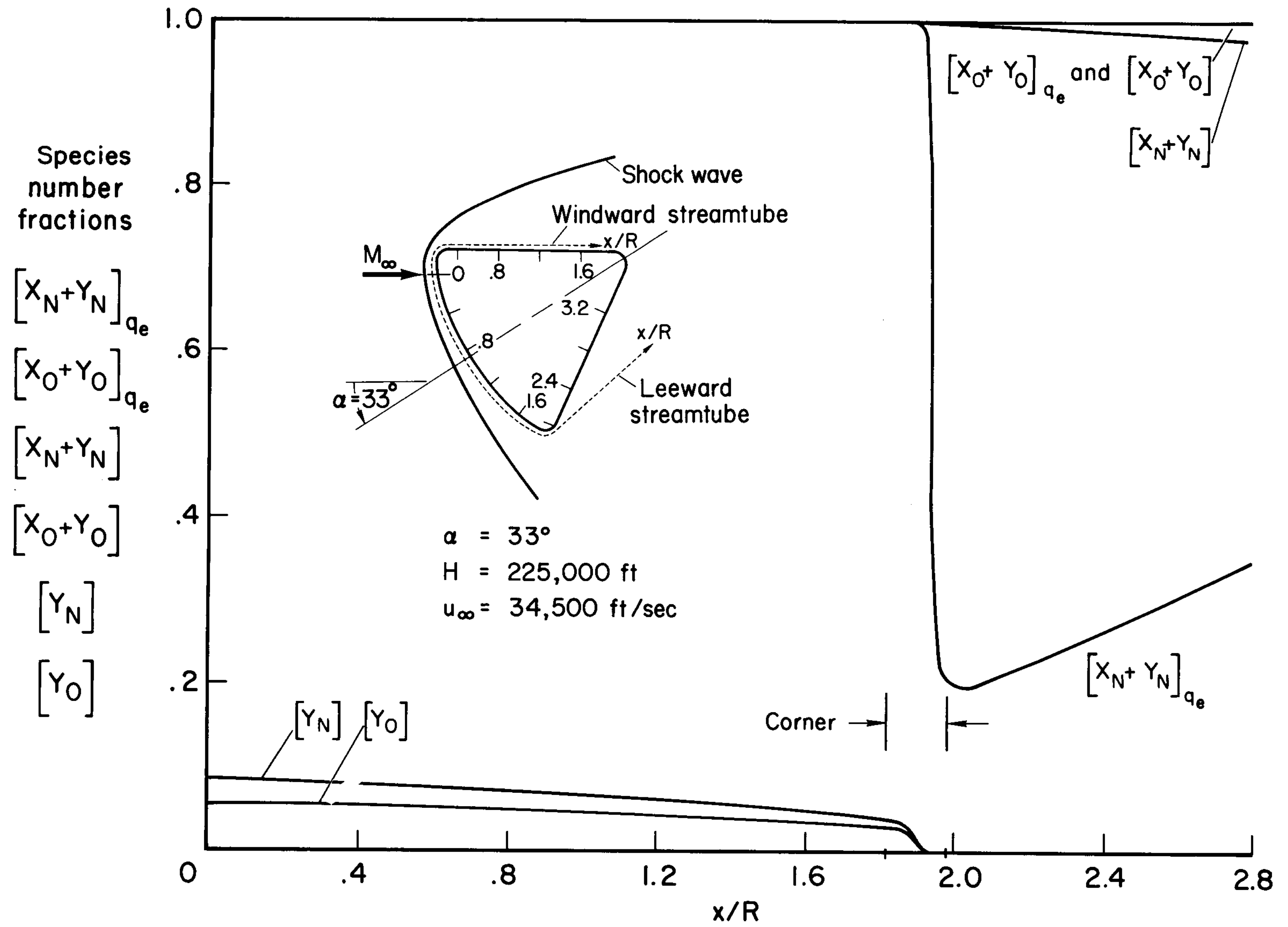

(a) Leeward side, overshoot trajectory.

Figure 12.- Species fractions along a streamtube close to the surface of full-scale vehicle for peak heating conditions along several trajectories.

[redacted]

[redacted]SSIFIED

[redacted]

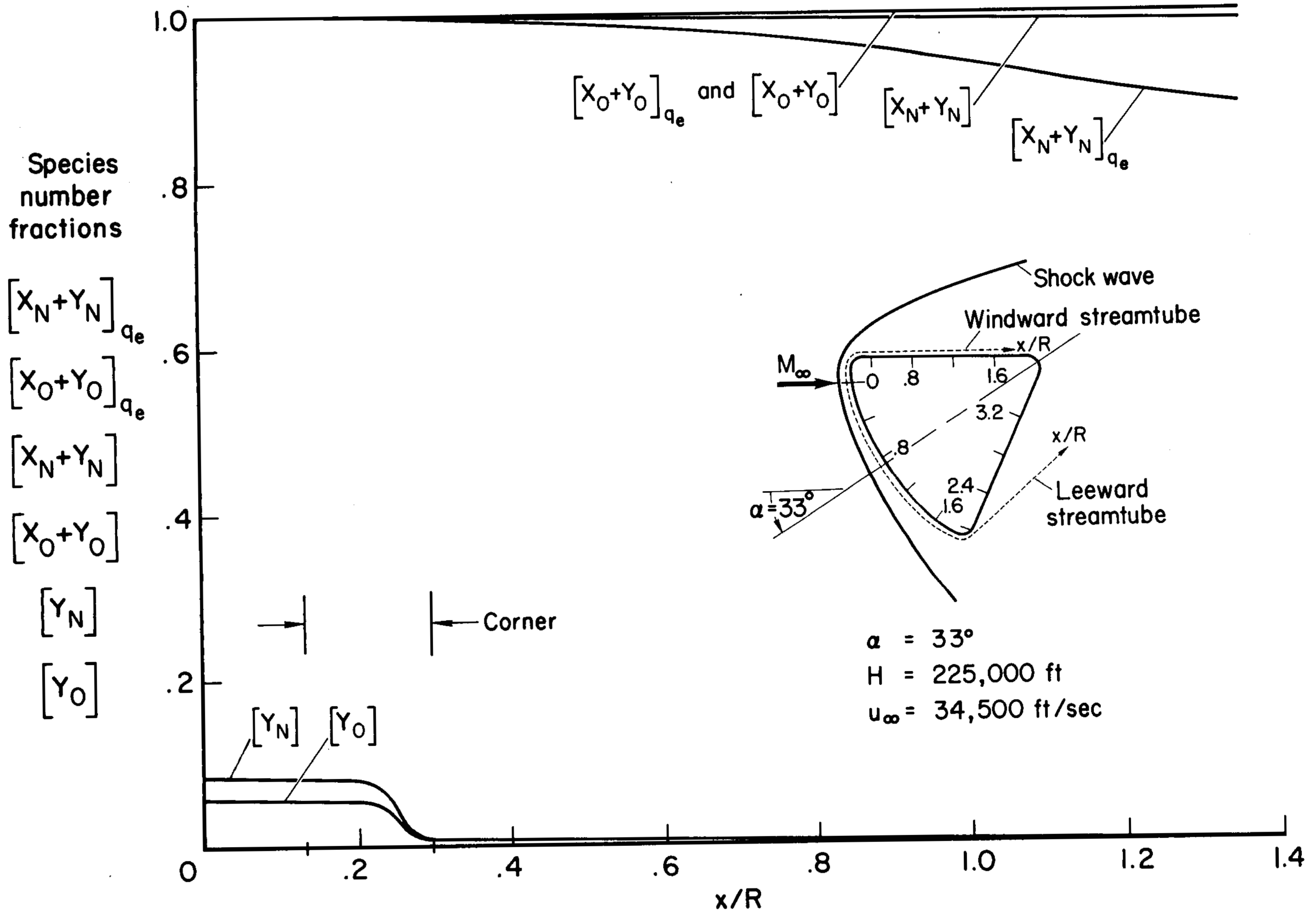

(b) Windward side, overshoot trajectory.

Figure 12.- Continued.

[redacted]

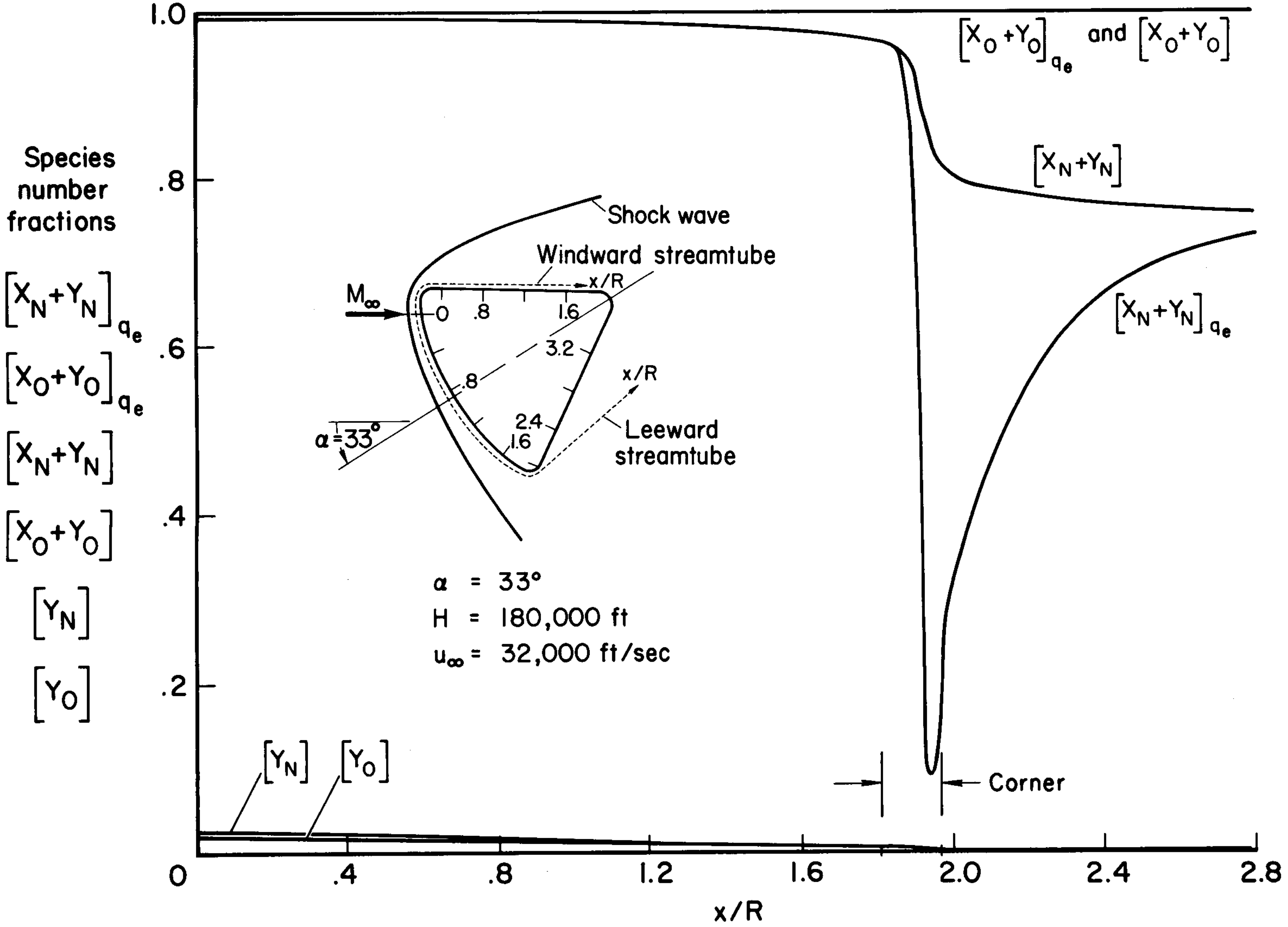

(c) Leeward side, undershoot trajectory.

Figure 12.- Continued.

[redacted]

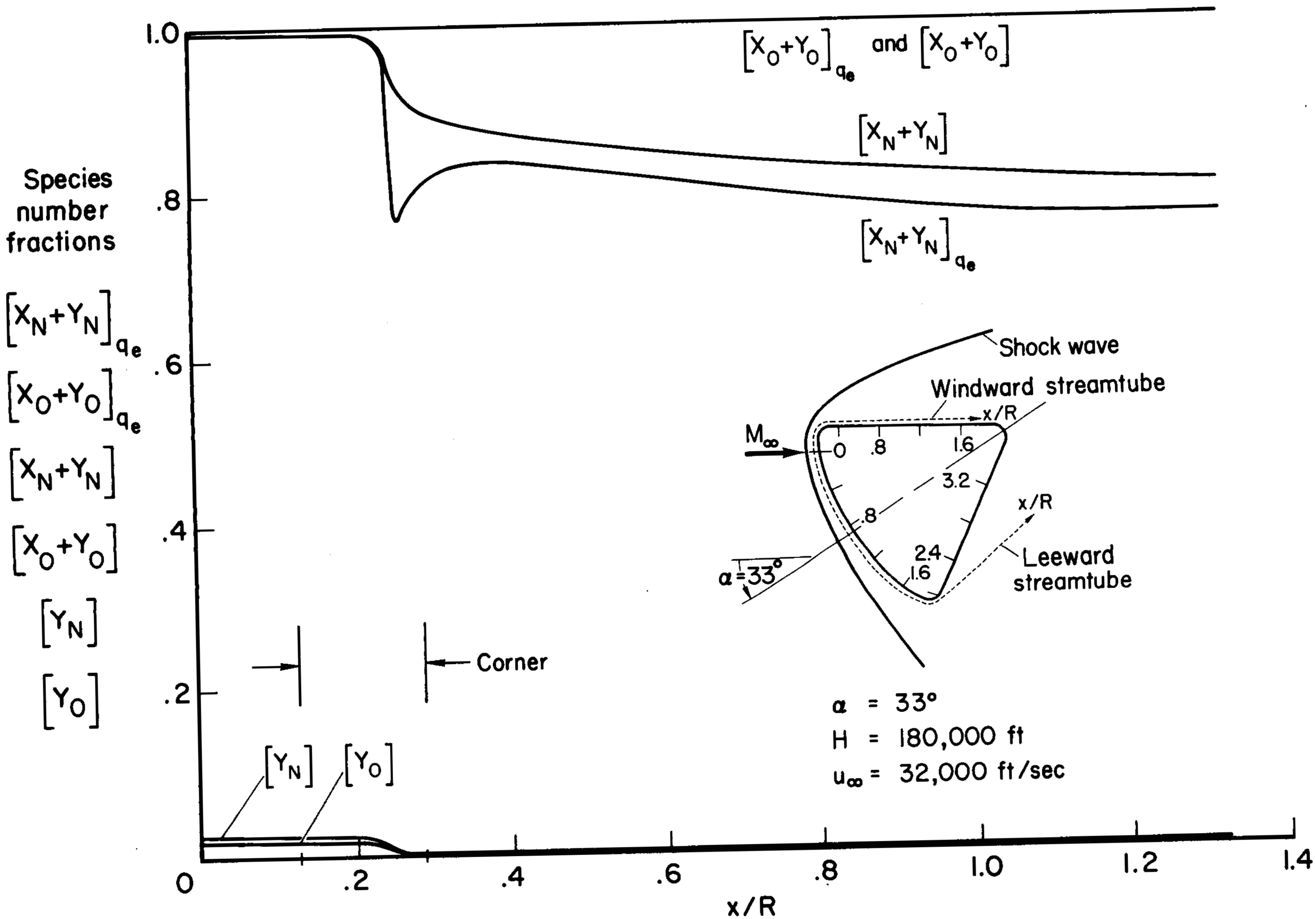

(d) Windward side, undershoot trajectory.

Figure 12.- Continued.

[redacted]SSIFIED

[redacted]

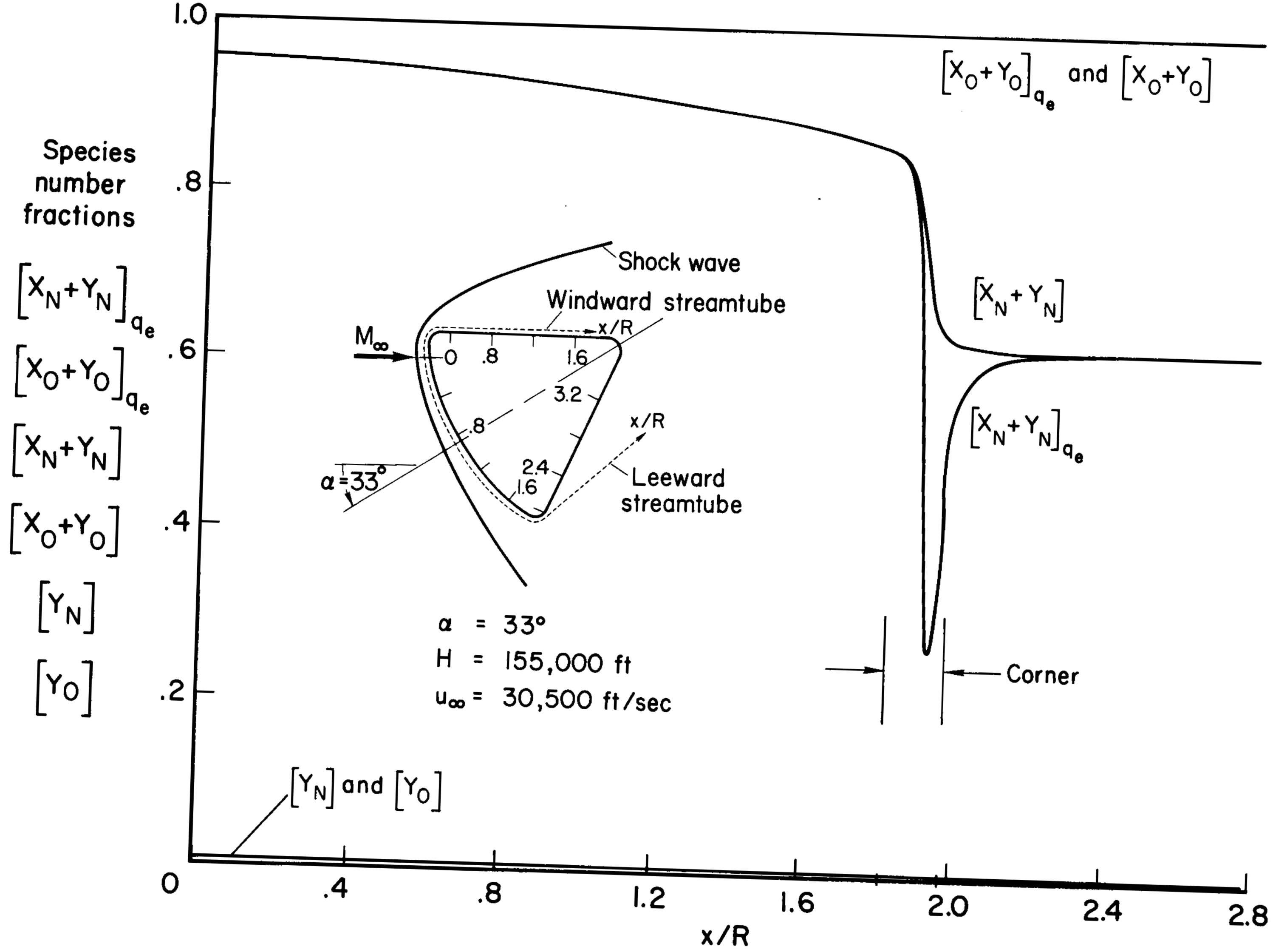

(e) Leeward side, emergency trajectory.

Figure 12. - Continued.

[redacted]

DE[redacted]SSIFIED

[redacted]

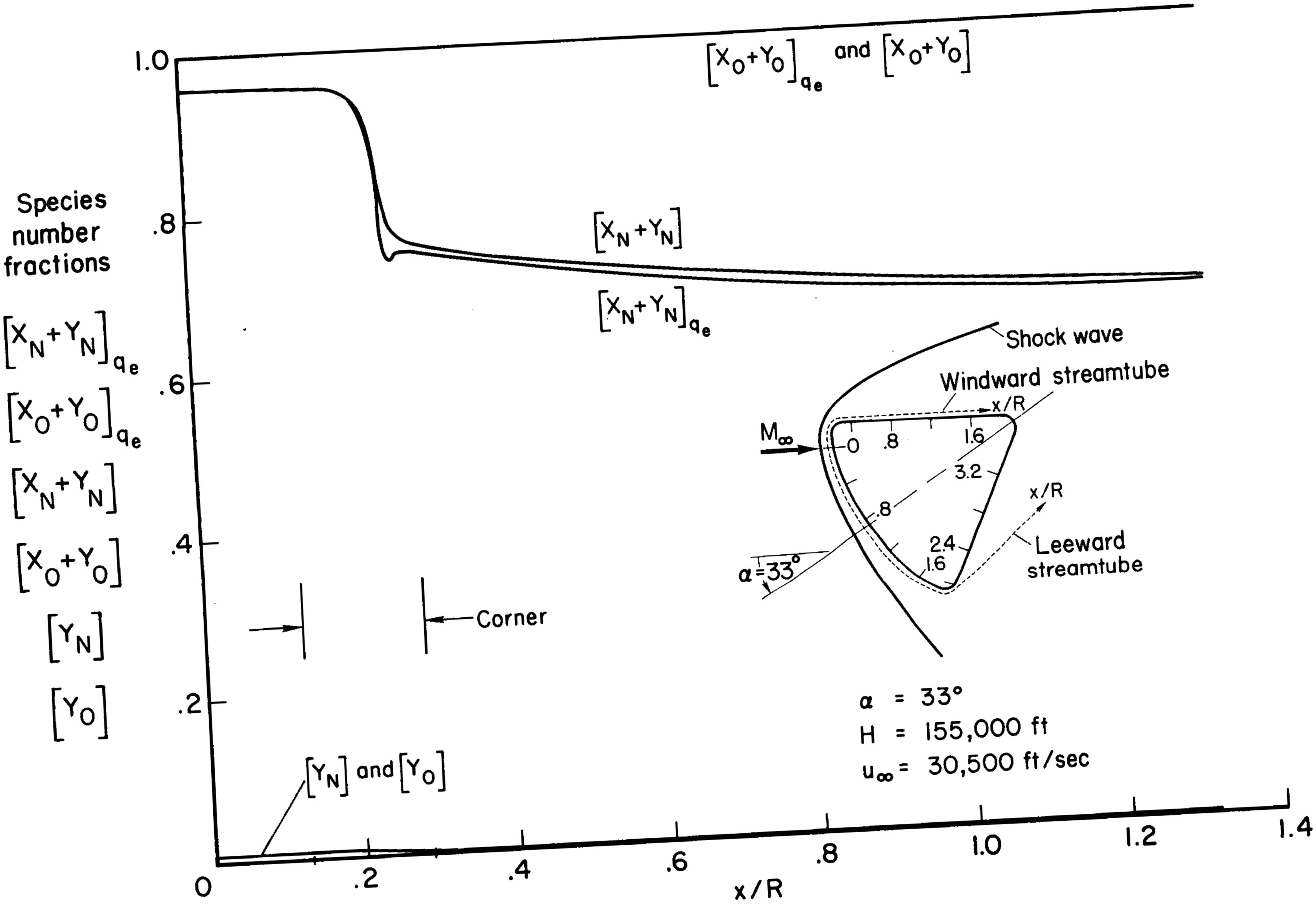

(f) Windward side, emergency trajectory.

Figure 12.- Concluded.

[redacted]

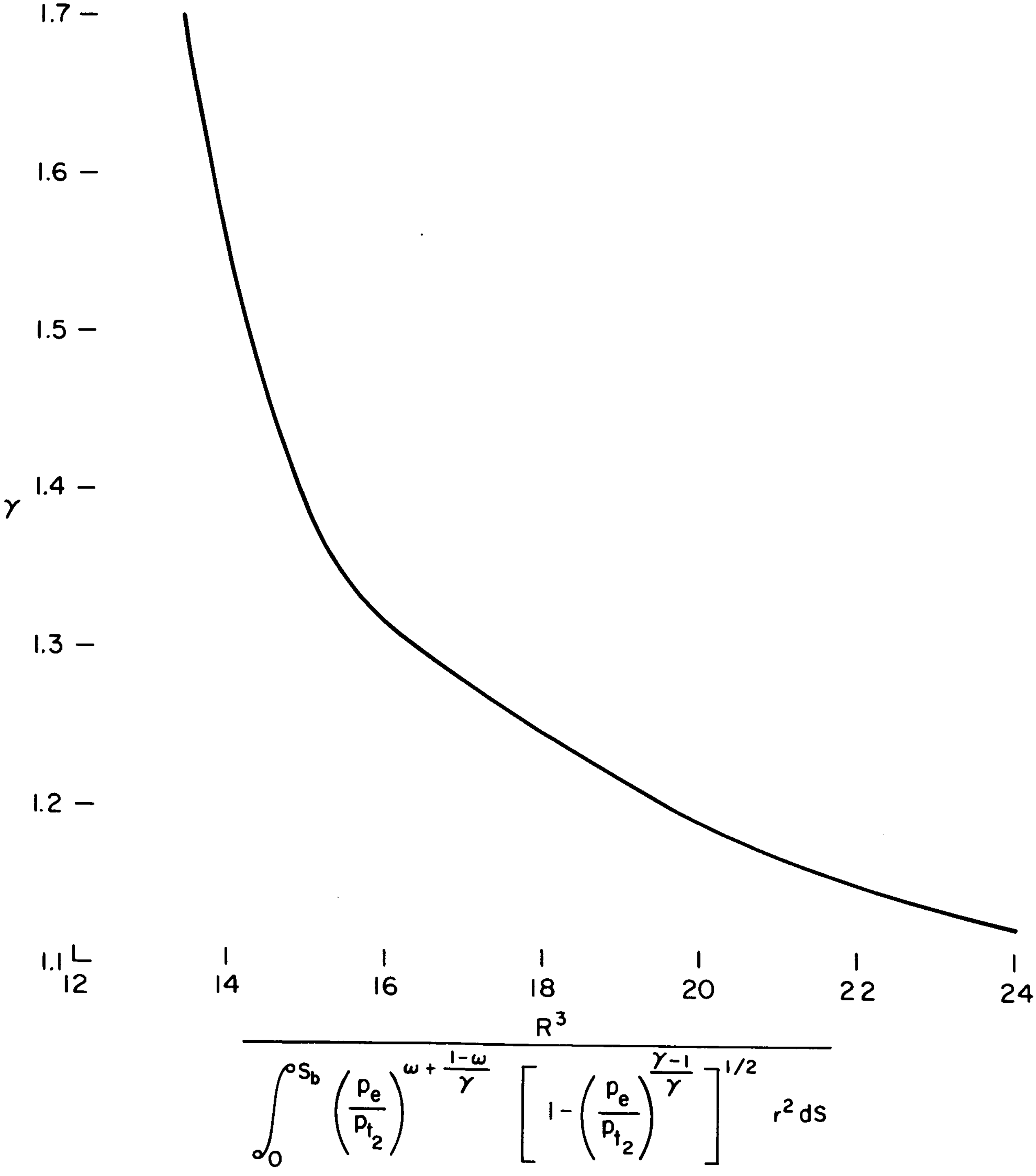

Figure 13.- Value of denominator in equation (A3).

[redacted]

NASA-Langley, 1966 A-2210